Monthly Notices
of the
ROYAL ASTRONOMICAL SOCIETY

MNRAS **450,** 3270–3288 (2015) doi:10.1093/mnras/stv748

Proper motions and kinematics of selected bulge globular clusters

L. J. Rossi,[1] S. Ortolani,[2,3] B. Barbuy,[4★†] E. Bica[5] and A. Bonfanti[2]

[1]*Centre for Astrophysics and Supercomputing, Swinburne University of Technology, Hawthorn, Victoria 3122, Australia*
[2]*Dipartimento di Fisica e Astronomia, Università di Padova, I-35122 Padova, Italy*
[3]*INAF-Osservatorio Astronomico di Padova, Vicolo dell'Osservatorio 5, I-35122 Padova, Italy*
[4]*Departamento de Astronomia, Universidade Federal do Rio Grande do Sul, CP 15051, Porto Alegre 91501-970, Brazil*
[5]*Universidade de São Paulo, IAG, Rua do Matão 1226, Cidade Universitária, São Paulo 05508-900, Brazil*

Accepted 2015 April 2. Received 2015 March 27; in original form 2014 September 27

ABSTRACT

We computed proper motions of a selected sample of globular clusters projected on the central bulge, employing CCD images gathered along the last 25 yr at the ESO-New Technology Telescope, ESO-Danish and *Hubble Space Telescope* telescopes. We presented a method to derive their proper motions, and a set of coordinate transformations to obtain 3D Galactic velocity vectors of the clusters. We analysed 10 globular clusters, namely Terzan 1, Terzan 2, Terzan 4, Terzan 9, NGC 6522, NGC 6558, NGC 6540, AL 3, ESO456−SC38 and Palomar 6. For comparison purposes, we also studied the outer bulge cluster NGC 6652. We discuss the general properties of the proper-motion-cleaned colour–magnitude Diagrams, derived for the first time for most of them. A general conclusion is that the inner bulge globular clusters have clearly lower transverse motions (and spatial velocities) than halo clusters, and appear to be trapped in the bulge bar.

Key words: Galaxy: bulge – globular clusters: individual: NGC 6522, NGC 6558, AL 3, HP 1, ESO456−SC38 (Djorgovski 2), NGC 6540 (Djorgovski 3), Terzan 1, Terzan 2, Terzan 4, Terzan 9, Palomar 6, NGC 6652.

1 INTRODUCTION

Globular clusters (GCs) in the Galactic bulge preserve in their spatial distribution and orbital evolution essential information to probe the early formation stages of the Galaxy central parts. The combination of dynamical properties of GCs, with their ages and chemical composition, provides a new tool to investigate the bulge stellar populations, and to build a consistent scenario of the Galactic bulge formation.

Stars and GCs in the Galactic halo present very elliptical orbits, with low angular momentum, while disc objects show circular orbits with high angular momentum, and small vertical velocity. The bulge instead shows an intermediate angular momentum, with higher perpendicular velocities than disc stars, but not going as deep into the halo as genuine halo stars. For the field bulge stars, kinematics reveals two different behaviours (Babusiaux et al. 2010): (1) a metal-poor component, enriched in [Mg/Fe], consistent with an isotropic rotating population belonging to an old spheroid, and (2) a metal-rich one with a vertex deviation consistent with that expected from a population with orbits supporting a bar. The spatial separation of these two components is not well determined. More recently, Babusiaux et al. (2014) and Zoccali et al. (2014) carried out large surveys on stars in the Galactic bar, inner disc and central bulge, by measuring radial velocities and metallicities from CaT lines, and traced the bar with more precision. Of interest to us is the conclusion that there is a concentration of metal-poor stars, that could have formed before the bar instability, and could have been trapped by the bar when it formed, staying confined in the innermost regions of the boxy bulge (Babusiaux et al. 2014; Di Matteo et al. 2014). Their conclusion is that the exact distribution of metal-poor stars, and their connection with the formation history of the thick disc, inner halo and the bar need further investigations.

Most of previous efforts in bulge cluster proper motion measurements were carried out using *Hubble Space Telescope* (*HST*) data as those e.g. by Zoccali et al. (2001) for NGC 6553, Feltzing & Johnson (2002) for NGC 6528, Bellini et al. (2013) for NGC 6338 and NGC 6441, and Kuijken & Rich (2002) for field stars. Ground-based large telescopes equipped with Multi-Conjugate Adaptive Optics also allowed proper-motion cleaning to be performed, such as those carried out by Ferraro et al. (2009) for Terzan 5, and Ortolani et al. (2011) for HP 1.

Calculations of Galactic orbits, based on proper motions and radial velocities, for some inner Galaxy clusters were carried out by Dinescu et al. (2003).

In previous works, we studied the inner bulge GCs, by means of colour–magnitude diagrams (CMDs) and spectroscopy

★E-mail: barbuy@astro.iag.usp.br
†Observations collected at the European Southern Observatory at La Silla, Chile; Proposals 087.D-0218(A), 089.D-0194(A), 091.D-0711(A), PI: S. Ortolani.

(e.g. Ortolani, Bica & Barbuy 1995; Barbuy, Bica & Ortolani 1998, 2009). We now have an unprecedented archive of CCD images taken since the 90s with European Southern Observatory (ESO) New Technology Telescope (NTT) and Danish telescopes, and the *HST*. Through the combination of this archive data with more recent CCD images, this data set allows cluster proper motions to be derived, and therefore proper-motion-cleaned CMDs and kinematics (e.g. Ortolani et al. 2011).

We focus on moderately metal-poor GCs ([Fe/H] ~ -1) with blue horizontal branch (HB), projected at low galactic latitude, because they might be the oldest population in the Galaxy (e.g. Barbuy et al. 2009). They might belong to the same generation of stars as the central RR Lyrae (Dékány et al. 2013), the latter identified as an old and spheroidal component of the bulge. We also study a few more metal-rich GCs.

Our main goal is to derive accurate ($\sim$0.5 mas yr^{-1}) absolute proper motions. Kinematic properties of the sample clusters should allow bulge members and halo intruders to be distinguished. The proper-motion results, coupled with radial velocities, allow 3D-orbit determinations in the Galactic potential (e.g. Ortolani et al. 2011). The orbits will be used to constrain different stellar-population components. In a forthcoming paper, the orbits will be presented in detail.

In this work, we derive the initial state vector for a total of 10 GCs. Section 2 describes the selection of the sample. In Section 3, we report the observations. In Section 4, proper motions are derived. In Section 5, we present an analysis of errors, the results are presented in Section 6 and conclusions are drawn in Section 7.

2 SAMPLE SELECTION

2.1 Metallicity and spatial distribution

The metallicity distribution of the Milky Way GCs is shown in Fig. 1, where metallicities are adopted from Bica et al. (2006), in some cases updated with more recent spectroscopic analyses (Barbuy et al. 2009, 2014).

Fig. 1 shows a Gaussian distribution centred around [Fe/H] $\simeq -1.6$, representing the metal-poor population, and a Gaussian distribution around the value [Fe/H] $\simeq -0.55$, corresponding to the metal-rich population (e.g. Kinman 1959; Morgan 1959; Zinn 1985; Côté 1999). A moderately metal-poor subpopulation characterized by [Fe/H] $\simeq -1.0$ is evident (see also Côté 1999).

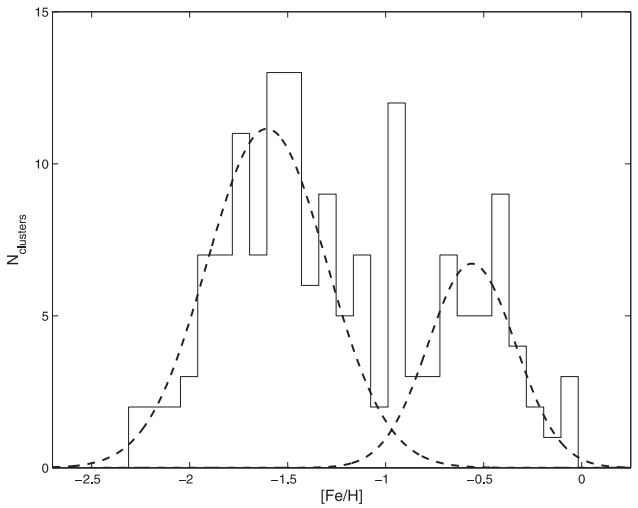

Figure 1. Metallicity distribution of the Milky Way GCs, updated with recent literature. Dashed lines are Gaussian fits for the metal-rich and metal-poor populations.

With this criterion in mind, we subdivided the GCs into three subsamples:

(i) metal-poor GCs (95 objects): [Fe/H] < -1.1,
(ii) metal-rich GCs (42 objects): [Fe/H] > -0.9, and
(iii) moderately metal-poor GCs (13 objects): $-1.1 \leq$ [Fe/H] $- \leq -0.9$.

In this work, we prioritize clusters with a blue HB together with a metallicity of [Fe/H] ~ -1.0, including NGC 6522, NGC 6558, AL 3, ESO456−SC38, NGC 6540. We also study two mainly red horizontal branch and moderately metal-poor clusters, Terzan 1 and Palomar 6, two metal-poor GCs projected on the inner bulge (Terzan 4, Terzan 9), and one metal rich (Terzan 2). For comparison purposes, we also included the outer bulge NGC 6652, with proper motion values taken from Sohn et al. (2014).

The log of observations is presented in Table 1. In Table 2, we report the cluster distances from the literature. This Table shows a good agreement among authors, which gives confidence on the distance values.

2.2 The distance of the Galactic Centre

The distance of the Sun from the Galactic Centre ($R_\odot$) is a crucial parameter that we use to establish a cluster initial state vector.

One of the most common methods adopted to determine the value of this parameter is the determination of the mean distance of Galactic GCs (Bica et al. 2006), or the distribution of RR Lyrae stars (Dékány et al. 2013). Another method is based on the distribution of field clump stars (Nishiyama et al. 2006; Cao et al. 2013; Bobylev et al. 2014). Finally, Gillessen et al. (2009), and Do et al. (2013) reported recent values from the orbit of stars around SGR A*, and derived a geometrical distance. A recent review of these methods and results was presented by Malkin (2013). The distances of the Sun to the Galactic centre essentially vary from 7.5 to 8.5 kpc. In this paper, we considered both 7.5 kpc, for the reason that this distance is consistent with the distribution of bulge GCs, and 8.3 kpc, as reported by Brunthaler et al. (2011), Schönrich (2012), Reid et al. (2014) and Hou & Han (2014), among others. In Table 3, we give the proper motion values, and Galactic distance components and velocity vectors, computed for both $R_\odot = 7.5$ kpc, and $R_\odot = 8.3$ kpc (see Section 4).

2.3 Distribution of clusters in the Galaxy

Fig. 2 shows the Galactocentric-distance distribution of the three metallicity subsamples of GCs. Figs 3 and 4 show the Galactic distribution of the three subsamples. The coordinates of the clusters are expressed in the inertial right-handed Galactocentric frame of reference, in which the x-axis points towards the Sun. The model of the Galactic bar and of the spiral pattern have been chosen according to Pichardo, Martos & Moreno (2004) and Pichardo et al. (2003), respectively. In Figs 2–4, we used a Galactocentric distance of $R_\odot = 7.5$ kpc.

We identified the following features of the three subsamples. Metal-poor clusters are distributed in a nearly spherical volume with a radius of about 30 kpc, consistently with a halo population. The spatial distribution of metal-rich clusters is more centrally concentrated than the metal-poor ones, as expected. The moderately

Table 1. Log of observations of first and second epochs.

Cluster	Telescope	Instrument	Date	Filter	Exposure	Seeing
Terzan 1 1st	Danish	0.47 arcsec pixel^{-1}	06/1990	*I*	180 s	1.1
	Danish	0.47 arcsec pixel^{-1}	06/1990	Gunn *z*	120 s	1.1
Terzan 1 2nd	NTT	EFOSC2 0.24 arcsec pixel^{-1}	05/2012	*I*	10 s	1.1
	NTT	EFOSC2 0.24 arcsec pixel^{-1}	05/2012	Gunn *z*	180 s	1.1
Terzan 2 1st	NTT	SUSI 0.13 arcsec pixel^{-1}	05/1994	*V*	30,720 s	0.8, 0.9
	NTT	SUSI 0.13 arcsec pixel^{-1}	05/1994	*I*	60,420 s	0.8, 0.8
Terzan 2 2nd	NTT	EFOSC2 0.24 arcsec pixel^{-1}	06/2011	*V*	60,300,20 s	1.1,1.1,1.1
	NTT	EFOSC2 0.24 arcsec pixel^{-1}	06/2011	*I*	40,180,10 s	1.1,1.1,1.1
Terzan 4 1st	NTT	SUSI 0.13 arcsec pixel^{-1}	05/1994	*V*	60,600 s	0.55, 0.55
	NTT	SUSI 0.13 arcsec pixel^{-1}	05/1994	*I*	60,300 s	0.4,0.4
	NTT	SUSI 0.13 arcsec pixel^{-1}	05/1994	Gunn *z*	120 s	0.5
Terzan 4 2nd	NTT	EFOSC2 0.24 arcsec pixel^{-1}	05/2012	*I*	30 s	0.6
	NTT	EFOSC2 0.24 arcsec pixel^{-1}	05/2012	*V*	30 s	0.6
Terzan 9 1st	Danish	DFOSC 0.39 arcsec pixel^{-1}	07/1998	*V*	60,900,60 s	1.3,1.3,1.3
	Danish	EFOSC2 0.39 arcsec pixel^{-1}	07/1998	*I*	60,90 s	1.1,1.1
Terzan 9 2nd	NTT	DFOSC 0.24 arcsec pixel^{-1}	05/2012	*V*	30,90 s	0.5,0.7
	NTT	EFOSC2 0.24 arcsec pixel^{-1}	05/2012	*I*	10,20 s	0.55,0.6
NGC 6522 1st	*HST*	WFPC2	09/1995	*F439W*	50,160,160 s	–
	HST	WFPC2	09/1995	*F555W*	10,50 s	–
NGC 6522 1st	Danish	0.47 arcsec pixel^{-1}	06/1992	*V*	60,480 s	1.2,1.3
	Danish	0.47 arcsec pixel^{-1}	06/1992	*I*	20,300 s	1.2,1.2
NGC 6522 2nd	NTT	EFOSC2 0.24 arcsec pixel^{-1}	05/2012	*V*	30,60 s	0.55,0.75
	NTT	EFOSC2 0.24 arcsec pixel^{-1}	05/2012	*I*	15,30 s	0.5,0.7
NGC 6558 1st	NTT	EMMI 0.35 arcsec pixel^{-1}	06/1993	*I*	7,120 s	1.2,1.2
	NTT	EMMI 0.35 arcsec pixel^{-1}	06/1993	*V*	10,180 s	1.2,1.2
NGC 6558 2nd	NTT	EFOSC2 0.24 arcmin pixel^{-1}	05/2012	*V*	90,300 s	0.6,0.6
	NTT	EFOSC2 0.24 arcmin pixel^{-1}	05/2012	*I*	60,180,20 s	0.5,0.55,0.55–0.6
NGC 6540 1st	Danish	0.47 arcsec pixel^{-1}	06/1990	*V*	60 s	1.3
	Danish	0.47 arcsec pixel^{-1}	06/1990	*I*	15 s	1.0
NGC 6540 2nd	NTT	EFOSC2 0.24 arcsec pixel^{-1}	05/2012	*V*	30 s	0.9
	NTT	EFOSC2 0.24 arcsec pixel^{-1}	05/2012	*I*	10 s	0.9
AL 3 1st	Danish	DFOSC 0.39 arcsec pixel^{-1}	03/2000	*V*	60,180 s	1.2,1.2
	Danish	DFOSC 0.39 arcsec pixel^{-1}	03/2000	*I*	10,40 s	1.2,1.2
AL 3 2nd	NTT	EFOSC2 0.24 arcsec pixel^{-1}	05/2012	*V*	30,60,240,60 s	0.6 for all
	NTT	EFOSC2 0.24 arcsec pixel^{-1}	05/2012	*I*	10,30,180 s	0.6
ESO456−SC38 1st	NTT	SUSI 0.13 arcsec pixel^{-1}	05/1994	*I*	60 s	0.9
	NTT	SUSI 0.13 arcsec pixel^{-1}	05/1994	*V*	180 s	0.8
	NTT	SUSI 0.13 arcsec pixel^{-1}	05/1994	Gunn *z*	60 s	0.8
ESO456−SC38 2nd	NTT	EFOSC2 0.24 arcsec pixel^{-1}	05/2012	*V*	900,60 s	1.0,1.0
	NTT	EFOSC2 0.24 arcsec pixel^{-1}	05/2012	*I*	30 s	0.8
Palomar 6 1st	NTT	EMMI 0.35 arcsec pixel^{-1}	06/1993	*V*	900 s	1.4
	NTT	EMMI 0.35 arcsec pixel^{-1}	06/1993	*I*	300 s	1.4
Palomar 6 2nd	NTT	EFOSC2/HR 0.12 arcsec pixel^{-1}	05/2013	Gunn *z*	300 s	0.9
	NTT	EFOSC2/HR 0.12 arcsec pixel^{-1}	05/2013	*I*	300 s	1.1

metal-poor subsample is confined within the inner 5 kpc of the Milky Way.

In order to identify the clusters located in the Galactic bulge, we selected a region on the celestial sphere included between $|l| \leq 18^{\circ}$ and $|b| \leq 7.5^{\circ}$. The metallicity distribution of the 39 clusters located in this region of the sky is shown in Fig. 5. The moderately metal-poor clusters show a peak comparable to that of the metal-rich clusters.

In Fig. 6, we show the projection of their coordinates on the Galactic plane and on the $x-z$ plane, where a distance to the Galactic centre of $R_{\odot} = 7.5$ kpc was adopted. They appear centrally concentrated, and possibly trapped within the bar.

3 OBSERVATIONS

The first epoch archival data are based on the ESO NTT telescope, obtained in 1993 and 1994, the ESO Danish 1.5 m telescope in 1990, 1998 and 2000, and the *HST*. The latter observations were acquired in 1995, under the proposal GO 9065, PI: S. Djorgowski, and the photometry is available as reported in Piotto et al. (2002).[1]

The NTT 1993 data used the EMMI (ESO Multi-mode instrument) spectrograph/focal reducer equipped with the CCD Loral

[1] http://www.astro.unipd.it/globulars/

Table 2. Distances from the literature (all values in kpc).

Cluster	Bica+06	Valenti+07	Harris96	Barbuy+98	Other	Reference
Terzan 1	6.2	6.6	6.7	4.90	5.2	Ortolani et al. (1999b)
Terzan 2	8.7	7.4	7.5	6.64	7.7	Ortolani, Bica & Barbuy (1997c)
Terzan 4	9.1	6.7	7.2	7.28	8.0	Ortolani, Bica & Barbuy (1997b); Ortolani et al. (2007)
Terzan 9	7.7	5.6	7.1	–	4.9	Ortolani, Bica & Barbuy (1999a)
NGC 6522	7.8	7.4	7.7	6.05	6.2	Barbuy, Ortolani & Bica (1994)
NGC 6558	7.4	–	7.4	–	6.3	Rich et al. (1998)
NGC 6540	3.7	5.2	5.3	3.02	3.5	Bica, Ortolani & Barbuy (1994)
AL 3	–	–	6.5	–	6.0	Ortolani, Bica & Barbuy (2006)
ESO456−SC38	6.7	7.0	6.3	3.02	5.5	Ortolani, Bica & Barbuy (1997a)
Palomar 6	7.3	–	5.8	–	8.9	Ortolani et al. (1995)
NGC 6652	9.6	–	10.0	–	9.3	Ortolani, Bica & Barbuy (1994)

Table 3. Kinematical properties. Upper panel: input data; lower panel: derived Galactocentric vectors and velocities, and literature metallicities; first and second lines correspond to distance of the Sun to the Galactic centre of 7.5 and 8.3 kpc.

CLUSTER	α (°)	δ (°)	l (°)	b (°)	μ_α^* (mas yr^{-1})	μ_δ (mas yr^{-1})	v_r (km s^{-1})	$d_\odot$ (kpc)
Terzan 1	263.95	−30.47	357.57	1.00	0.51 ± 0.31	−0.93 ± 0.29	114.0 ± 14.0	6.2 ± 0.6
Terzan 2	261.89	−30.80	356.32	2.30	−0.94 ± 0.30	0.15 ± 0.42	109.0 ± 15.0	8.7 ± 0.8
Terzan 4	262.66	−31.59	356.02	1.31	3.50 ± 0.69	0.35 ± 0.58	−50.0 ± 2.9	9.1 ± 0.9
Terzan 9	270.41	−26.84	3.61	−1.99	0.00 ± 0.38	−3.07 ± 0.49	59.0 ± 10.0	7.7 ± 0.7
NGC 6522	270.89	−30.03	1.02	−3.93	3.35 ± 0.60	−1.19 ± 0.34	−21.1 ± 3.4	7.8 ± 0.7
NGC 6558	272.57	−31.76	0.20	−6.02	−0.12 ± 0.55	0.47 ± 0.60	−197.2 ± 1.5	7.4 ± 0.7
NGC 6540	271.53	−27.76	3.29	−3.31	0.07 ± 0.40	1.90 ± 0.57	−17.72 ± 1.4	3.7 ± 0.3
AL 3	273.53	−28.63	3.36	−5.27	4.77 ± 0.46	0.55 ± 0.44	–	6.5 ± 0.6
ESO 456–SC38	270.45	−27.83	2.77	−2.50	3.08 ± 0.29	2.00 ± 0.34	–	6.7 ± 0.6
Palomar 6	265.93	−26.22	2.10	1.78	2.95 ± 0.41	1.24 ± 0.19	181.0 ± 2.8	7.3 ± 0.7
NGC 6652	278.94	−32.99	1.53	−11.38	4.75 ± 0.07	−4.45 ± 0.10	−111.7 ± 5.8	9.6 ± 0.9

CLUSTER	X (kpc)	Y (kpc)	Z (kpc)	$\dot{X}$ (km s^{-1})	$\dot{Y}$ (km s^{-1})	$\dot{Z}$ (km s^{-1})	[Fe/H]
Terzan 1	1.3	0.3	0.1	−125 ± 14	−25 ± 18	−24 ± 9	−1.3
	(2.1)	(0.3)	(0.1)	(−125)	(−45)	(−24)	
Terzan 2	−1.2	0.6	0.4	−122 ± 15	18 ± 22	−26 ± 14	−0.5
	(−0.4)	(0.6)	(0.4)	(−122)	(−10)	(−25)	
Terzan 4	−1.6	0.6	0.2	46 ± 3	121 ± 32	132 ± 31	−1.6
	(−0.8)	(0.6)	(0.2)	(46)	(92)	(133)	
Terzan 9	−0.2	−0.5	−0.3	−76 ± 10	99 ± 25	−58 ± 16	−1.0
	(0.6)	(−0.5)	(−0.3)	(−76)	(54)	(−57)	
NGC 6522	−0.3	−0.1	−0.5	20 ± 4	−11 ± 22	−129 ± 22	−0.86
	(0.5)	(−0.1)	(−0.5)	(23)	(−36)	(−127)	
NGC 6558	0.1	0.0	−0.8	184 ± 3	−12 ± 26	32 ± 20	−0.97
	(0.9)	(0.0)	(−0.8)	(184)	(−36)	(32)	
NGC 6540	3.8	−0.2	−0.2	8 ± 2	−155 ± 19	20 ± 8	−1.0
	(4.6)	(−0.2)	(−0.2)	(8)	(−167)	(20)	
AL 3	1.0	0.4	−0.6	–	–	–	−1.3
	(1.8)	(0.4)	(−0.6)	(−)	(−)	(−)	
ESO 456–SC38	0.8	0.3	−0.3	–	–	–	−0.5
	(1.6)	(0.3)	(−0.3)	(−)	(−)	(−)	
Palomar 6	0.2	−0.3	0.2	−195 ± 3	85 ± 23	76 ± 18	−1.0
	(1.0)	(−0.3)	(0.2)	(−195)	(62)	(77)	
NGC 6652	−1.9	−0.3	−1.9	150 ± 8	169 ± 19	−256 ± 28	−0.81
	(−1.1)	(−0.3)	(−1.9)	(150)	(138)	(−255)	

ESO #34, of 2048 × 2048, giving a 0.35 arcsec pixel^{-1} scale. The NTT 1994 images employed the Superb-seeing Imager (SUSI) camera equipped with the CCD ESO #25, with 0.13 arcsec pixel^{-1} scale. The Danish 1.5 m 1990 images employed the direct focal camera with CCD ESO # 5, of 512 × 320 30 μm pixels, of scale 0.47 arcsec pixel^{-1}. The Danish 1.5m 1998 and 2000 data come from the DFOSC spectrograph/focal reducer equipped with the Loral/Lesser C1W7 2052 × 2052 15 μm pixels, with scale 0.39 arcsec pixel^{-1}.

The second-epoch observations were obtained with the ESO NTT+EFOSC2 instrument, in V, I and Gunn z. The CCD ESO # 40 UV-flooded, of 2048 × 2048, with 15 μm pixels was used, giving a projected scale of 0.12 arcsec pixel^{-1}. The total field has 4.1 arcmin × 4.1arcmin. In the 2011 and 2012 observations, the CCD was read in 2×2 pixel binned mode, which gives the best duty cycle observing time. In 2013, the full resolution was used, because of its higher astrometric accuracy and higher dynamical range.

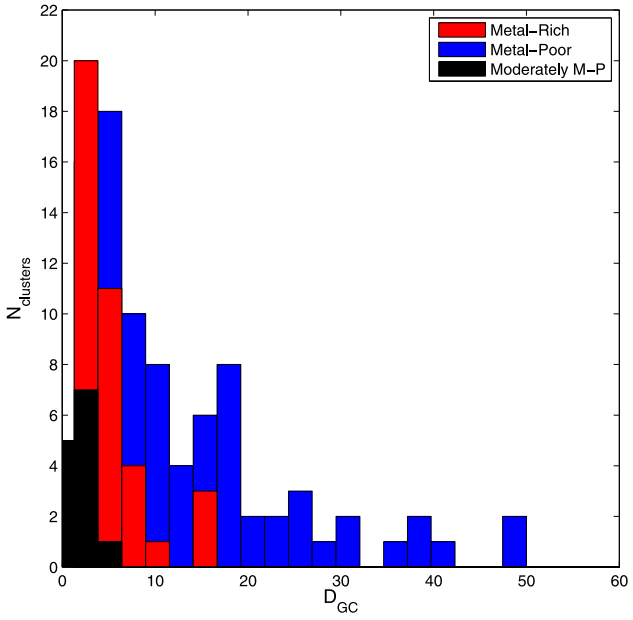

Figure 2. Galactocentric distance (in kpc) distribution of the three subsamples of GCs.

The log of observations for the two epochs (Table 1) summarize the essential information on the data.

4 PROPER MOTION DERIVATION

We describe below the method applied to derive the proper motions of the sample. The basic idea is to transform the coordinates of cluster and field stars in the two different epochs, into a common frame of reference (main-frame) and compute the proper motion in terms of coordinate changes in the main-frame. The configuration of stars in the two epochs in principle should be different because of the different proper motion of single stars. Therefore, a suitable choice of the stars to be used to determine the coordinate transformation is required. We assumed that cluster members have similar proper motion and, because of the gravitational bound, they maintain a similar configuration in the two epochs. We used the cluster members to determine the coordinate transformation in the main-frame and subsequently we applied the same transformation to all stars, both field and cluster. In this work, we chose second epoch images as main-frame. Subtracting the value of the coordinates of stars in the second epoch image from those in the first, we expect to find (if the cluster has a significant proper motion) two distinct aggregations of stars in the $(\Delta x, \Delta y)$ plane: one centred around $(\Delta x, \Delta y) = (0, 0)$ (the cluster) and the other around another point different from the origin (the field).

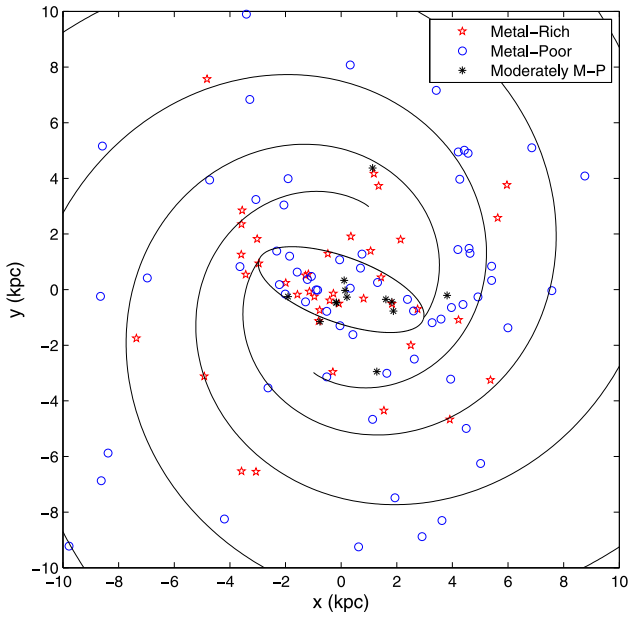

Figure 3. Spatial distribution of GCs projected on the Galactic plane on the $x-y$ plane, viewed from the North Galactic Pole.

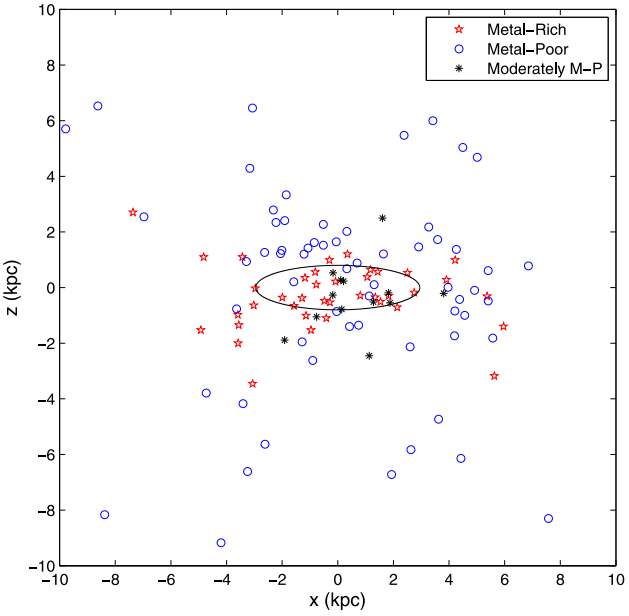

Figure 4. Spatial distribution of GCs projected on the $x-z$ plane for a selection of $|l| \leq 18^{\circ}$ and $|b| \leq 7.5^{\rm circ}$.

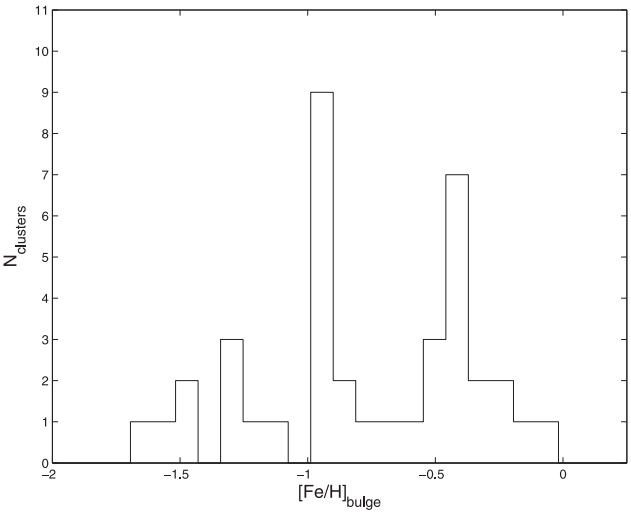

Figure 5. Metallicity distribution of the GCs projected on the Galactic bulge.

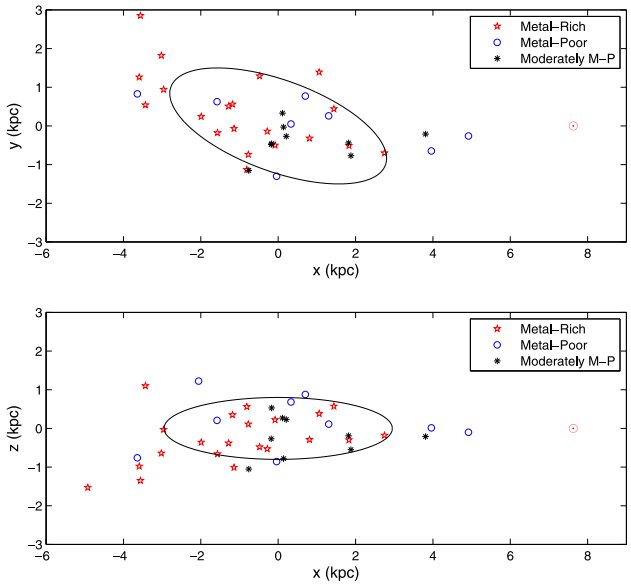

Figure 6. Spatial distribution of Galactic bulge GCs overlapped on the central bar model.

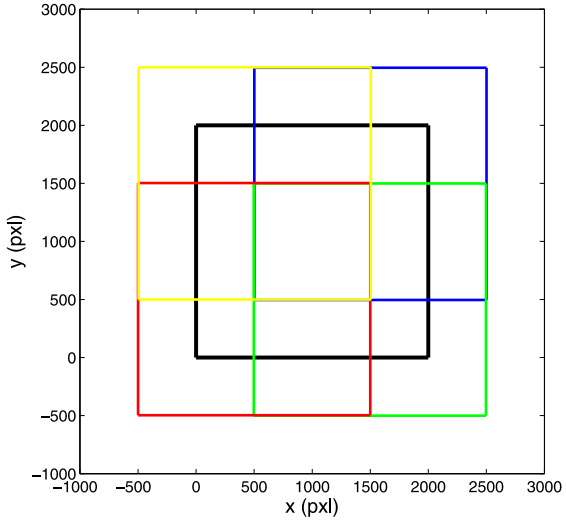

Figure 7. Dither pattern of four of the eight images used to evaluate the field-distortion.

4.1 The technique for computing proper motions

The raw data have been pre-processed, using MIDAS commands, trimming the images and subtracting the bias. Many tests have been carried out on the flat-fields obtained during the same observing runs, both inside the dome and on the sky twilight, and the latter proved to be better distributed. An average of 10 flats have been used for the flat-field correction. We used the code DAOPHOT (Stetson 1987) for the point spread function (PSF) photometry choosing a uniform number of bright and isolated stars for the average reference PSF used for fitting. A two degree polynomial was used across the field accounting for the PSF variations in the second epoch NTT+EFOSC2 data. Some crowded fields needed a local subtraction of faint, close-by sources to the reference stars used to model the PSF. The fitting was performed using the ALLSTAR routine which generates the relative photometry, the refined positions of the centroids and other parameters useful to clean the generated list from spurious objects or bad measurements. This routine creates the `.als` tables that we used as starting data for the proper motions.

We used single-image data after several tests on the selected best images, as compared with the average of multiple observations. This is due to the peculiarity of the targets that are very crowded and contaminated. The quality of the results is more dependent on the resolution (seeing, focus, tracking), and the capability to isolate the cluster CMD sequences, rather than on the number of used frames. In addition, in most cases, the errors are dominated by the first epoch, where only a single colour image was available.

The stars in common in the two images have been identified and sorted out using the codes `DAOMATCH` and `DAOMASTER`. In the following analysis, we use the quantities

(i) (x_1, y_1): coordinates of the star (in pixels) in the first image,
(ii) (x_2, y_2): coordinates of the star (in pixels) in the second image,
(iii) (x_1^t, y_1^t), (x_2^t, y_2^t): coordinates of the star (in pixels) in the main-frame, obtained applying the transformation, and
(iv) $(\Delta x, \Delta y) = (x_2^t - x_1^t, y_2^t - y_1^t)$: difference in the position of the star in the main-frame in the two epochs.

4.1.1 *Field distortion and coordinate transformation*

Before proceeding further with the description of the present technique to compute proper motions, we propose an analysis of the effects of the field distortion. In fact, the distortion of star positions is a systematic effect that has to be treated carefully. A systematic displacement of the coordinates might result in a misinterpretation of the proper motions. A first solution to minimize this effect is to select stars in the central regions of the CCD, where the distortion is expected to be lower than in the peripheral regions. As discussed below, the field distortion is the reason why a conformal transformation including shift, rotation and scale is not enough to transform the coordinates in the two epochs into the main-frame.

We evaluated the field-distortion affecting the second-epoch images from the NTT (for the first epoch we do not have distortion maps available). In particular, we reduced a set of images of a field located in the Baade's Window with uniformly distributed stars including a central frame and eight shifted images of the same field. The shift of the eight images is 60 arcsec, corresponding to approximately 500 pixels, both in right ascension and/or in declination, depending on the image. Fig. 7 shows the dithering pattern for the four images shifted both in right ascension and declination. For a better visualization of the dithering pattern, we did not show the configuration of the images shifted only in right ascension or declination. We identified stars in common in all nine frames (419 stars) and computed the distortion vector for each star. We selected as main-frame of reference the system of coordinates of the central image. According to Anderson & King (2003), in order to transform the coordinates of the shifted images into the main-frame we applied a conformal transformation on the coordinates of the stars in the shifted images,

$$\begin{bmatrix} x_i^t \\ y_i^t \end{bmatrix} = \lambda \begin{bmatrix} \cos\theta & \sin\theta \\ -\sin\theta & \cos\theta \end{bmatrix} \begin{bmatrix} x_i \\ y_i \end{bmatrix} + \begin{bmatrix} x_0 \\ y_0 \end{bmatrix}, \quad (1)$$

where (x_i, y_i) are the coordinates of the stars in each shifted frame, (x_i^t, y_i^t) are the transformed coordinates, λ is the scale parameter, θ is the rotation parameter and (x_0, y_0) are the shift parameters.

We computed the mean position of each star in the central frame of reference as follows:

$$\begin{cases} \bar{x} = \dfrac{x_{\rm c} + \sum_{i=1}^{8} x_i^{\rm t}}{9} \\ \bar{y} = \dfrac{y_{\rm c} + \sum_{i=1}^{8} y_i^{\rm t}}{9} \end{cases}, \tag{2}$$

where $(x_{\rm c}, y_{\rm c})$ are the coordinates of each star in the central image. Our main assumption is that the mean position computed represents a good approximation of the distortion-free coordinates of the stars, justified by the fact that we obtained an isotropic dithering pattern. The field distortion has been evaluated by subtracting the coordinates in each shifted image to the mean coordinates. We then assumed that the distortion map can be well represented by a third-order-polynomial transformation of the form

$$\begin{cases} \Delta x(x, y) = a_{00} + a_{10}x + a_{01}y + a_{20}x^2 + a_{11}xy + a_{02}y^2 \\ \qquad\qquad a_{30}x^3 + a_{21}x^2y + a_{12}xy^2 + a_{03}y^3 \\ \Delta y(x, y) = b_{00} + b_{10}x + b_{01}y + b_{20}x^2 + b_{11}xy + b_{02}y^2 \\ \qquad\qquad b_{30}x^3 + b_{21}x^2y + b_{12}xy^2 + b_{03}y^3 \end{cases}. \tag{3}$$

We derived the (a_{ij}, b_{ij}) coefficients by fitting the distortion model to the computed distortion vectors. The top panel of Fig. 8 shows the distortion model for NTT derived from this analysis, with distortion vectors magnified by a factor 40. The central and the bottom panels show the values of our model of $(\Delta x, \Delta y)$ as a function of the (x, y) coordinates on the CCD. The field-distortion is lower in the CCD centre than in the peripheral regions, where the distortion of a star coordinates can be up to about 2 pixels.

In order to test the reliability of the field-distortion model, we applied the correction to the stellar positions of the nine exposures of the Baade's Window. We recalculated the mean position of the stars in the main-frame using conformal transformation and evaluated the residuals $(\mathrm{d}x, \mathrm{d}y)$ between the main-frame average position and those of the single exposures transformed on the main-frame as a function of the (x, y) main-frame positions (see Fig. 9). Note that the displacement is constant to a good approximation along the whole CCD and we conclude that the third-order-polynomial transformation produces a good distortion model. Given that the clusters in our images are located approximately at the centre of the detector, thus with minimal distortions, in order to minimize the effects of the distortion, we obtained the proper motions by selecting field stars included within a circular area between 500 and 1500 pixels both in x and y, centred on the cluster. We test if in this region of the detector the field, distortion can be well represented by a polynomial transformation of second order. The most important reason for such an order decrease is that, for some sample clusters, the number of cluster members available to calculate coordinate transformation between the two epochs is low. Decreasing the order will result into a more robust evaluation of the transformation coefficients. Following this approach, we considered only the central frame and evaluated the distortion model by applying the same procedure described above, decreasing the order of the transformation to the second power. Fig. 10 shows the analogue results of Fig. 9 for the central regions of the CCD after correcting the coordinates with a second order transformation. Also in this case the displacement is constant for every value of (x, y) and we can conclude that the distortion map in the inner regions is well represented by a second-order polynomial model.

Having derived a field-distortion model for all second-epoch exposures from NTT+EFOSC2, we test if a quadratic transformation is sufficient to transform the coordinates of the first-epoch images in

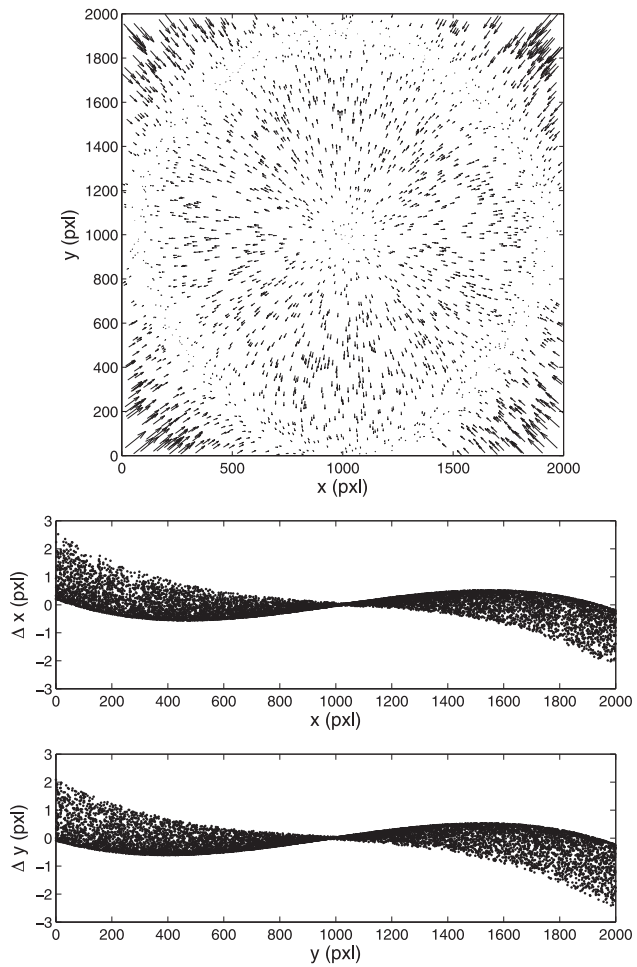

Figure 8. Top panel: model of the field distortion for NTT. For a better visualization, the distortion vectors are magnified by a factor 40. Central and middle panels: field distortion as function of the (x, y) coordinates.

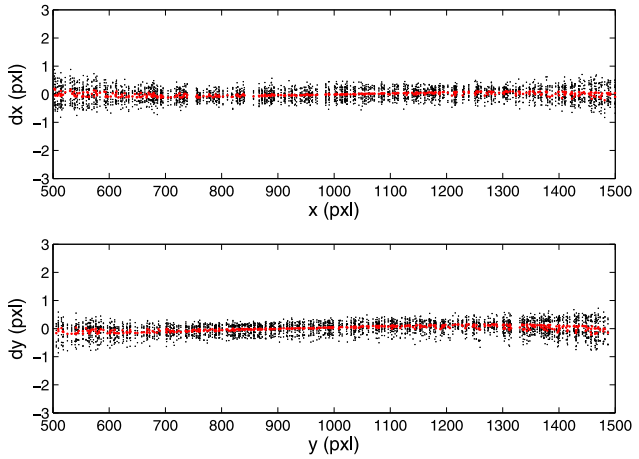

Figure 9. Residuals of the position of the stars after correction for field-distortion as function of the mean coordinates. The red dots represent the average of the displacement.

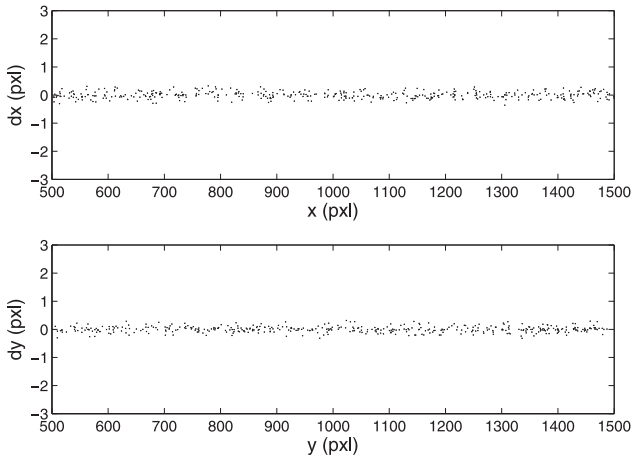

Figure 10. Residuals of the position of the stars in the central frame after correcting for field-distortion with a second order polynomial transformation as function of the mean coordinates.

the frame of reference of the second-epoch for all other instruments used in this work. Explicitly

$$\begin{cases} x_1^{\rm t} = a_1\,{x_1}^2 + a_2\,x_1 y_1 + a_3\,{y_1}^2 + a_4\,x_1 + a_5\,y_1 + a_6 \\ y_1^{\rm t} = b_1\,{x_1}^2 + b_2\,x_1 y_1 + b_3\,{y_1}^2 + b_4\,x_1 + b_5\,y_1 + b_6 \end{cases} \quad (4)$$

$$\begin{cases} x_2^{\rm t} = x_2 + \Delta x_{\rm fd}(x_2, y_2) \\ y_2^{\rm t} = y_2 + \Delta y_{\rm fd}(x_2, y_2) \end{cases}, \quad (5)$$

where (x_1, y_1) are the raw positions of the stars in the first-epoch exposure, $(x_1^{\rm t}, y_1^{\rm t})$ are the coordinates of the first-epoch exposure transformed in the field-distortion-corrected second-epoch frame of reference, (x_2, y_2) are the raw positions of the stars in the second epoch exposure and $(\Delta x_{\rm fd}, \Delta y_{\rm fd})$ are the corrections for field-distortion of the second-epoch exposures. We performed the following tests.

(i) *Test 1*: apply our model of field-distortion correction to the second-epoch exposure. Use quadratic transformations to bring the first-epoch exposure raw positions on the second-epoch reference frame and measure the displacement between cluster members and field stars.

(ii) *Test 2*: apply the field-distortion to both the first-epoch and second-epoch exposures. Use a conformal transformation to bring the first-epoch coordinates in the frame of reference of the second-epoch image and measure the displacement between cluster members and field stars.

If the two methods give consistent results, we should be confident about the correctness of our approach. In the sample studied, the only case with known field-distortion for the first epoch is NGC 6522 from *HST*. In particular, we adopted the geometric-distortion solution proposed by Anderson & King (2003) for WFPC2. Fig. 11 shows the results of this analysis. The displacement obtained from *test 1* is $(\Delta x, \Delta y) = (0.24 \pm 0.04, 0.10 \pm 0.03)$ pixel, while *test 2* produced the values $(\Delta x, \Delta y) = (0.26 \pm 0.05, 0.14 \pm 0.04)$ pixel. In this case, we evaluated the displacement by fitting a double Gaussian to the data points. Considering the errors associated with our measurements, we see that the results of the two methods are consistent and a quadratic transformation is sufficient.

More specifically, we computed the transformation of coordinates in an iterative process. We identified in the two-epoch images a circular area centred on the cluster. As discussed above, the radius of such a circular area has been chosen in such a way as to

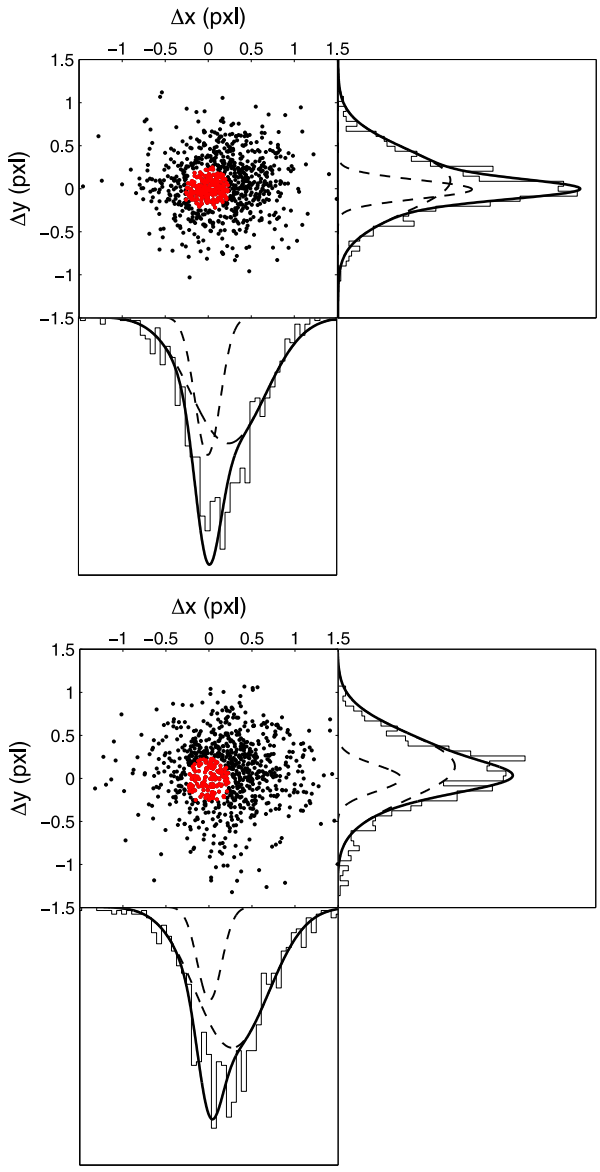

Figure 11. Displacement (in pixels) of NGC 6522 derived from *test 1* (upper panel) and *test 2* (bottom panel). The black dots are the field stars, while the red dots are the cluster members.

minimize the effects of the field distortion. In order to estimate, to a first approximation, the value of the coefficients of the coordinate transformation, we had to identify some stars likely belonging to the cluster. We based our choice on some features of the CMD. In particular, we assumed that most of the blue HB stars are cluster members. In the cases in which the HB was not well defined or absent, we selected the bright red giant branch (RGB) stars as cluster members. After the first fit based on the HB/RGB members, we employed an iterative process. We applied the transformation to the whole sample of stars and plotted their position in the $(\Delta x, \Delta y)$ plane. The cluster members were selected as the stars included within a circular area centred on the origin of the coordinates. The radius of the selection was chosen making sure that the selected stars were mostly located around the cluster evolutionary sequences of the CMD. We then computed again the coefficients of the transformation using the newly identified cluster members. We repeated this procedure iteratively until the value of the coefficients of the

coordinate transformation converged (we verified that usually four or five iterations were enough). This solution leads to two results: the determination of the proper motion of the cluster and the decontamination of the field stars from the cluster CMD.

4.1.2 Gaussian interpolation

Once the distribution of stars in the $(\Delta x, \Delta y)$ diagram is known, we determined the value of proper motion (in pixels) by means of an interpolation with a double Gaussian of the form

$$f(\Delta x) = A\exp\left[-\left(\frac{(\Delta x - \Delta x_{\rm cl})^2}{2\sigma_{\rm cl}^2}\right)\right] + B\exp\left[-\left(\frac{(\Delta x - \Delta x_{\rm field})^2}{2\sigma_{\rm field}^2}\right)\right], \quad (6)$$

where (A, B), $(x_{\rm cl}, x_{\rm field})$ and $(\sigma_{\rm cl}, \sigma_{\rm field})$ are the amplitude, the centre and the dispersion of the Gaussian describing the cluster stars and the field stars distribution on the Δx axis, respectively. The same was done for the distribution of stars along the Δy axis.

Finally the differences

$$\begin{cases} \Delta X = \Delta x_{\rm cl} - \Delta x_{\rm field} \\ \Delta Y = \Delta y_{\rm cl} - \Delta y_{\rm field} \end{cases} \quad (7)$$

give the cluster proper motion.

4.2 From proper motion to the state vector

We present a method to compute the state vector into the inertial Galactocentric frame of reference from proper motions, radial velocities and distances.

4.2.1 Absolute proper motion vector

Since we measure the proper motion of the cluster with respect to the bulge field stars (relative proper motion), in order to obtain the absolute proper motion of the cluster members we have to correct for the internal proper motion of the field stars. Ortolani et al. (2011) derived for the cluster HP 1 an internal proper motion of the bulge field stars equal to $v_T = 1.03\,{\rm kms}^{-1}$. Zoccali et al. (2001) assumed to measure the background field stars, having those in the near side moving on average in the opposite direction, with respect to those in the far side, because of bulge rotation, making that their overall proper motion is null. Terndrup et al. (1998) derived an internal proper motion $(\mu_{\rm l}, \mu_{\rm b})$=(0.2,0.2) mas yr^{-1}. We concluded that the correction for the internal proper motion is small if compared to the uncertainties associated with the proper motion of the cluster, so we will ignore it (see Ortolani et al. 2011).

4.2.2 Initial state vector

In order to predict the orbit of the cluster, we need the initial state vector, i.e. the initial conditions necessary for solving the system of differential equations represented by the equations of motion. The first step is to obtain the value of the velocity components of the cluster in the heliocentric frame of reference (U, V, W). We used a right-handed coordinate system, so that U, V, and W are positive in the direction of the Galactic centre, Galactic rotation and North Galactic Pole (NGP), respectively. We refer to Johnson & Soderblom (1987) for a more complete explanation of the procedure to obtain the heliocentric velocity vector starting from distance, proper motion and radial velocity. We adopted the value of

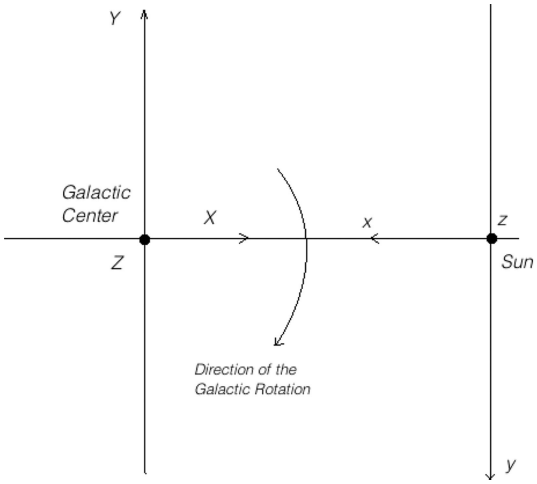

Figure 12. Inertial Galactocentric frame of reference (X, Y, Z) and non-inertial heliocentric frame of reference (x, y, z) configuration at the present time.

the velocity in the local standard of rest at the Sun's Galactocentric distance equal to $v_{\rm LSR} = 239.7\,{\rm kms}^{-1}$, according to Model III of Irrgang et al. (2013). The velocity components of the Sun with respect to the local standard of rest are (Schönrich, Binney & Dehnen 2010)

$$\begin{aligned} U_\odot &= 11.1 \pm 1 \text{ km s}^{-1} \\ V_\odot &= 12.24 \pm 0.2 \text{ km s}^{-1} \\ W_\odot &= 7.25 \pm 0.5 \text{ km s}^{-1} \\ |v_\odot| &= 18.04 \text{ km s}^{-1}. \end{aligned}$$

Thus, the Sun moves towards the Galactic centre and up towards the NGP away from the plane. It also moves around the Galactic centre faster than it would if it were on a circular orbit. The proper motion is then measured in the heliocentric frame of reference, which is not inertial (see Fig. 12). According to Terndrup et al. (1998), the perpendicular components of the velocity vector (y and z direction) expressed into the inertial heliocentric frame of reference is given by

$$\boldsymbol{v}_{\rm cl,\perp} = d_\odot \boldsymbol{\mu}_{\rm obs} + \boldsymbol{v}_{\odot,\perp}\left(1 - \frac{\rm d_\odot}{\rm d_f}\right), \quad (8)$$

where $d_\odot$ is the heliocentric distance of the cluster, $\boldsymbol{\mu}_{\rm obs}$ is the observed proper motion in Galactic coordinates, $d_{\rm f}$ is the heliocentric distance of the field stars and $\boldsymbol{v}_{\odot,\perp}$ are the perpendicular components of the velocity vector of the Sun with respect to the local standard of rest. Considering that the clusters we are studying are projected on the Galactic bulge, we assumed that

$$d_{\rm f} = {\rm R}_\odot, \quad (9)$$

where $\rm R_\odot$ is the Galactocentric distance of the Sun. Applying equation 8, we can write

$$\begin{cases} \dot{X} = -\left(U + U_\odot\right) \\ \dot{Y} = -\left[V + (v_{\rm LSR} + V_\odot)\left(1 - \frac{\rm d_\odot}{\rm R_\odot}\right)\right] \\ \dot{Z} = \left[W + W_\odot\left(1 - \frac{\rm d_\odot}{\rm R_\odot}\right)\right] \end{cases} . \quad (10)$$

The position vector of the cluster in the Galactocentric frame (X, Y, Z) is related to the measured position in the heliocentric frame of reference (x, y, z) by

$$\begin{cases} X = \mathrm{R}_\odot - x \\ Y = -y \\ Z = z. \end{cases} \quad (11)$$

5 ANALYSIS OF ERRORS

In this section, we describe the errors affecting our measurements.

5.1 Astrometric errors

Astrometric errors are the combination of different random and systematic errors. We identified several sources of uncertainty, namely the *random centring errors*, the *chromatic errors* (Ortolani et al. 2011) and the *field distortion errors*. We used images of the cluster NGC 6558 as a test case, but the results are valid in a more general context.

Centering error

We considered four images of NGC 6558 from NTT+EMMI (1993),

(i) V band, 10 s
(ii) V band, 3 min
(iii) I band, 7 s
(iv) I band, 5 min.

We selected the same region of the CCD used for the determination of the proper motion in each image and matched the `.als` tables with the `DAOMATCH` and `DAOMASTER` routines. We considered the I-band images to evaluate the centring error, because they are more populated than the images in the V band, leading to a better statistics. Furthermore, for most of the studied clusters, we used I-band images for the derivation of the proper motion. We designated the coordinates of the single star in the first image $(x_1, y_1)_i$ and in the second image $(x_2, y_2)_i$, with $i = 1$ to $\mathrm{N_{stars}}$ (hereafter i will be always intended in this range). The mean coordinates of the stars are

$$\begin{cases} \bar{x}_i = \dfrac{(x_1 + x_2)_i}{2} \\ \bar{y}_i = \dfrac{(y_1 + y_2)_i}{2} \end{cases} . \quad (12)$$

The standard deviation associated to this mean value is

$$\begin{cases} \sigma_x i = \left[\dfrac{(x_1 - \bar{x})_i^2 + (x_2 - \bar{x})_i^2}{2} \right]^{1/2} \\ \sigma_{y_i} = \left[\dfrac{(y_1 - \bar{y})_i^2 + (y_2 - \bar{y})_i^2}{2} \right]^{1/2} \end{cases} . \quad (13)$$

In Fig. 13, we show the error on the radial position of stars as a function of the instrumental I magnitude

$$\sigma_{\mathrm{R}i} = \sqrt{\sigma_{x_i}^2 + \sigma_{y_i}^2}. \quad (14)$$

We applied the same procedure for the I-band images from NTT+EFOSC (2012) and the results are shown in Fig. 14.

The order of magnitude of the average value of the astrometric error is about 0.1 pixel. Taking into account the number of about 1000 stars used for the derivation of the proper motions of the clusters, the order of magnitude of the centring error is as small as 10^{-3} pixel.

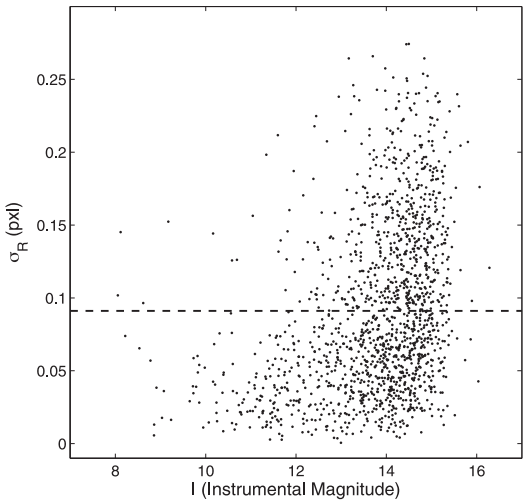

Figure 13. Centering error versus I-band instrumental magnitude for the 1993 images (NTT+EMMI). The dashed line shows the average astrometric error.

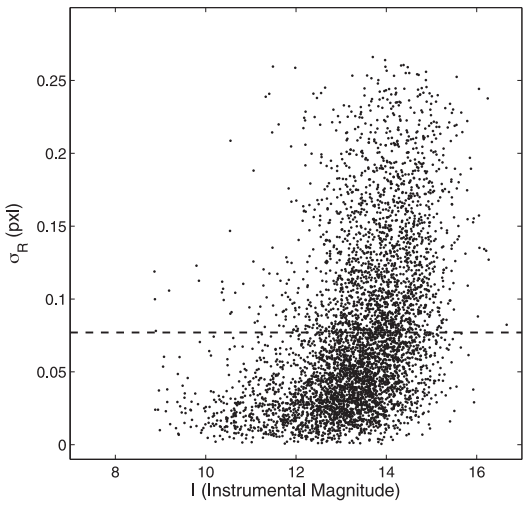

Figure 14. Centering error versus I-band instrumental magnitude for the 2012 images (NTT+EFOSC). The dashed line shows the average astrometric error.

Chromatic error

Chromatic errors are due to differential chromatic refraction (DCR), both atmospheric and instrumental, on stars with different colours at different air masses. The refraction dependence on wavelength (inverse quadratic to the first approximation) makes this effect more pronounced in the $(V - I)$ colour than in the near-infrared. In order to study the displacement of the stars as a function of their colours, we subdivided the sample of stars into 'red' and 'blue' groups, evaluating the average astrometric error for both. We show the results for NGC 6558 (NTT+EMMI 1993) in Fig. 15. Note that the number of stars is lower than that of the previous figures as a consequence of the match of the I and V `.als` tables.

We associate to the chromatic error the quantity

$$\sigma_{\mathrm{Chr}} = |\bar{\sigma}_{\mathrm{C,r}} - \bar{\sigma}_{\mathrm{C,b}}|. \quad (15)$$

We expect to obtain a similar result for the 2012 images. It is important to notice that the chromatic effect is small if compared

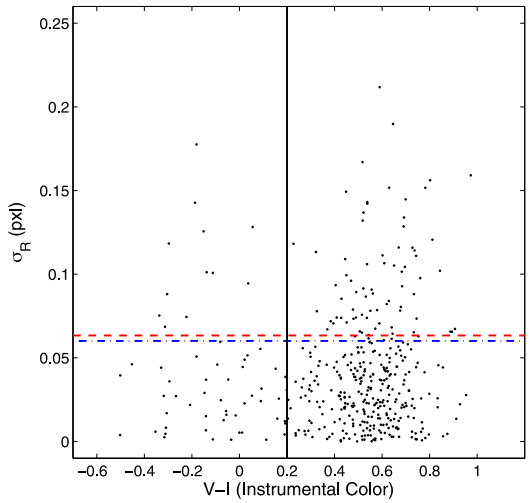

Figure 15. Centering error versus instrumental ($V - I$) colour. The red line shows the average centring error for the 'red' group, while the blue line shows the average centring error for the 'blue' group; these groups are separated by black vertical line.

with the centring error. In fact, the order of magnitude is 10^{-4} pixels, and then negligible.

We performed a further test in order to investigate the effects of DCR on our measured proper motions. We selected two clusters of our sample with detected blue HB stars, namely NGC 6540 (Fig. 23) and AL 3 (Fig. 24). In order to maximize the colour extension of the selection, we selected identified cluster members in a V range that contains both HB and RGB stars ($15.5 < V < 16.5$ for NGC 6540 and $14.5 < V < 17$ for AL 3). We then analysed the value of the proper motion as a function of the star colours. Fig. 16 shows the results of this analysis. We fitted a regression line (continuous line) to the data points applying a linear least square interpolation and plotted the regression lines (dashed lines) associated with the 95 per cent confidence bound on the coefficient values of the fit model. The right ascension component of NGC 6540 shows the highest dependence of the proper motion on the stars' colour. The declination components of NGC 6540 and both the right ascension and declination components of AL 3 show a very low dependence on the colour. However, if we consider the uncertainties associated with the regression model, we note that all the fitted lines are consistent with no slope within the errors. We can conclude that we did not find any significant dependence of the proper motion on the star colours and hence that we can confidently exclude a strong DCR effect on our data. The same conclusion was reached in Ortolani et al. (2011).

5.2 Gaussian interpolation error

The error associated with the double Gaussian interpolation is

$$\begin{cases} \sigma_{\Delta X} = \sqrt{\sigma^2_{\Delta x_{\rm cl}} + \sigma^2_{\Delta x_{\rm field}}} \\ \sigma_{\Delta Y} = \sqrt{\sigma^2_{\Delta y_{\rm cl}} + \sigma^2_{\Delta y_{\rm field}}} \end{cases}, \tag{16}$$

where $\Delta x_{\rm cl}$, $\Delta x_{\rm field}$, $\Delta y_{\rm cl}$, $\Delta y_{\rm field}$ are the uncertainties in the position of the cluster and field stars centroids in the (ΔX, ΔY) diagram for the x and y coordinates, respectively. The uncertainties associated with the astrometric and numerical errors are small if compared with

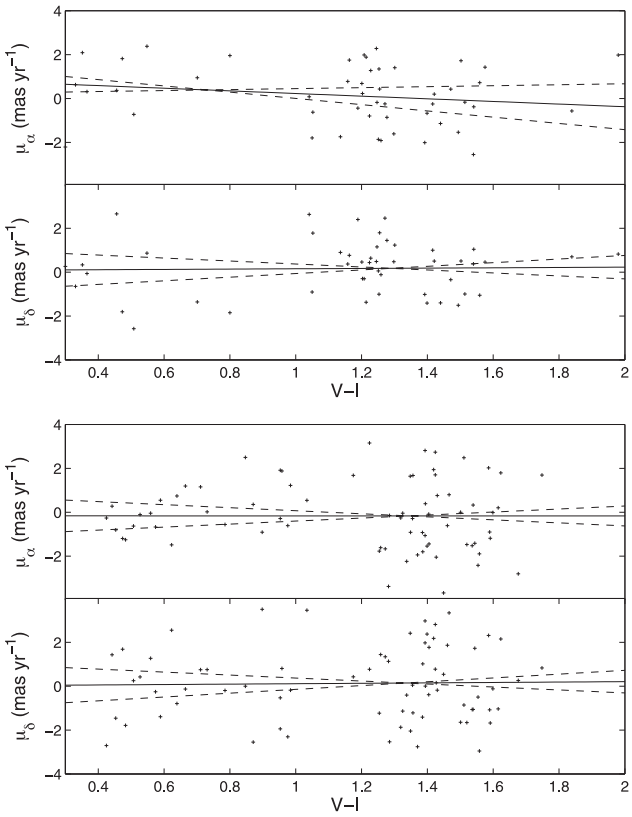

Figure 16. Components of the proper motion as function of the star colours for NGC 6540 (two panels) and for AL 3 (bottom two panels).

the uncertainties associated with the Gaussian interpolation, then we can neglect them and assume that the main source of uncertainty derives from this fitting procedure. This error is estimated directly from the routine that computes the coefficients of the Gaussian curve and coincides with the difference between the best-fitting value and the extremes of the 95 per cent confidence bounds.

Following Johnson & Soderblom (1987), we have all the ingredients to estimate the uncertainties in the velocity components. By applying the error-propagation to the estimate of the velocity components we found

$$\begin{bmatrix} \sigma^2_U \\ \sigma^2_V \\ \sigma^2_W \end{bmatrix} = \boldsymbol{C} \begin{bmatrix} \sigma^2_\rho \\ (k/\pi)^2 \left[\sigma^2_{\mu_\alpha} + (\mu_\alpha \sigma_\pi/\pi)^2\right] \\ (k/\pi)^2 \left[\sigma^2_{\mu_\delta} + (\mu_\delta \sigma_\pi/\pi)^2\right] \end{bmatrix} + \frac{2\mu_\alpha \mu_\delta k^2 \sigma^2_\pi}{\pi^4} \begin{bmatrix} b_{12} & b_{13} \\ b_{22} & b_{23} \\ b_{32} & b_{33} \end{bmatrix}. \tag{17}$$

The elements of the matrix $\boldsymbol{C}$ are the squares of the individual elements of $\boldsymbol{B}$, i.e. $c_{ij} = b^2_{ij}$ for all i and j (see Johnson & Soderblom 1987).

The final step to obtain the uncertainties associated with the state vector is to propagate the errors in position and velocity in the inertial Galactocentric frame of reference. This can be easily done computing the partial derivatives of the transformations of coordinates described in Section 4.

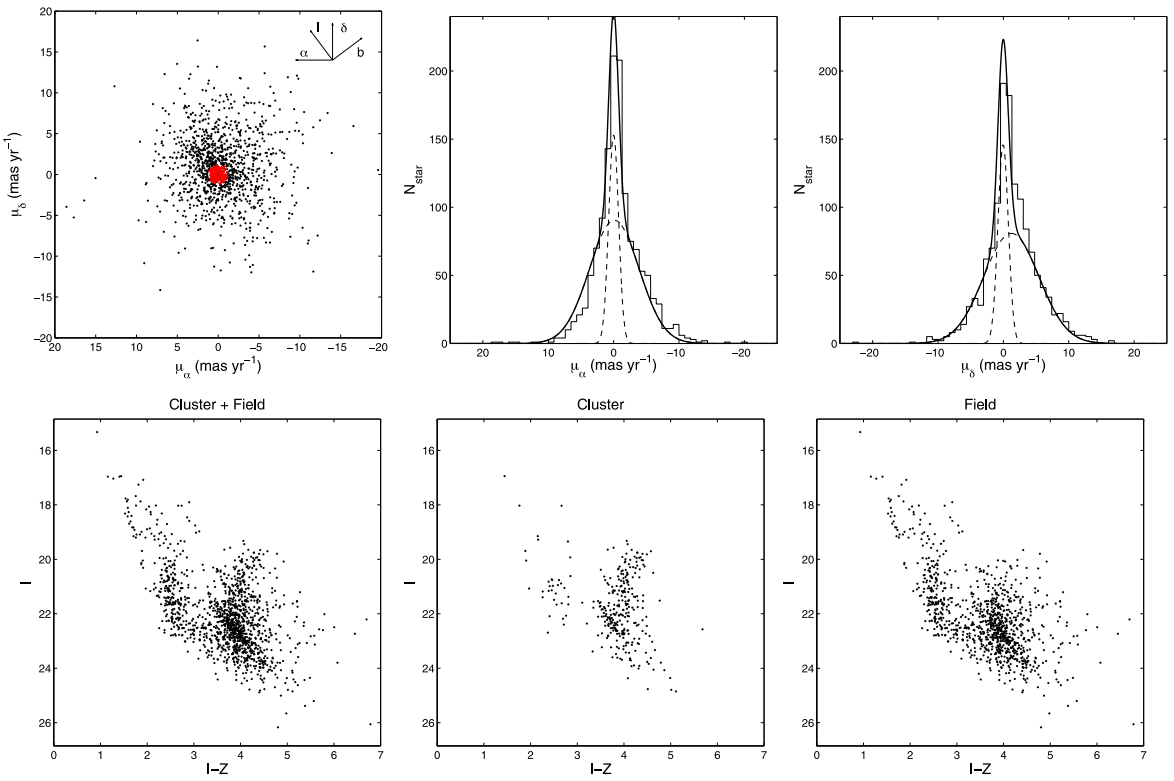

Figure 17. Proper motion and CMD decontamination of Terzan 1.

6 RESULTS FOR INDIVIDUAL GCS

We derived the proper motion of 10 bulge clusters. Table 3 gives the proper motion values, velocity components of the Galactocentric velocity vectors, and other relevant information. The input distances and coordinates for the sample clusters are from Bica et al. (2006). The data show that the proper motions and the velocity components of our targets are, on average, lower than those of halo clusters (e.g. Dinescu, Girard & van Altena 1999), with the exception of the two most metal-poor clusters (Terzan 4, Terzan 9). For the more reddened clusters Terzan 1, Terzan 4 and Palomar 6, we employed the z-band (instrumental), which provided a better definition to the CMDs. The studied clusters are discussed individually as follows.

Terzan 1

Terzan 1 is a moderately metal-poor ([Fe/H] ~ -1.0) GC with a dominant red HB. There is evidence that it is a second parameter GC showing a post-core collapse structure (Ortolani et al. 1999b). We used as first epoch the CCD camera on the Danish telescope observations taken in 1990 June, and as second epoch NTT+EFOSC2 data observed in 2012 May, with a baseline of 22 yr.

In Fig. 17 are shown the derived proper motions, the double-Gaussian interpolation of the displacements and the CMD cleaning of the cluster. The present analysis showed a small proper motion both in right ascension and declination, that could be an indication of the very elongated orbit of the cluster. This picture would be consistent with the relatively high radial velocity of Terzan 1 ($v_r = 114 \pm 14\,\mathrm{km\,s^{-1}}$; Idiart et al. 2002). The values are reported in Table 3.

Terzan 2

Terzan 2 is a metal-rich red HB cluster, located very close to the Galactic centre (Ortolani et al. 1997a; Valenti, Ferraro & Origlia 2007). With a baseline of 18 yr, a very good seeing and a good sampling in the first epoch observations, taken at NTT+SUSI, in 1994 May, the proper-motion cleaning is very satisfactory. The second epoch was taken with NTT+EFOSC2 in 2011 June. The cluster CMD given in Fig. 18 is not richly populated, but the elimination of field sequences was effective. Despite its location being among the closest objects to the Galactic centre, it shows a very low proper motion, below 1 mas yr^{-1}, together with a radial velocity of 109 km s^{-1}.

Terzan 4

Terzan 4 is among the most metal-poor clusters in the inner bulge (Ortolani et al. 1997b; Origlia & Rich 2004). First and second epoch observations were obtained, respectively, at the NTT+SUSI in 1994 May, and NTT+EFOSC2 in 2012 May. Both these sets of images have been obtained under exceptionally good seeing. The proper-motion-cleaned CMD with a baseline of 18 yr provided a very well defined RGB, as shown in Fig. 19. The definition of the CMD is comparable to that of NICMOS/*HST* one (Ortolani et al. 2007), showing the possibility of a few blue HB stars. The proper motion values, as well as the Galactic velocities (lower panel of Table 3) are somewhat higher than those of the sample average, possibly characterizing a halo-originated cluster (given also its much lower metallicity). The orbit prediction will bring more constraints.

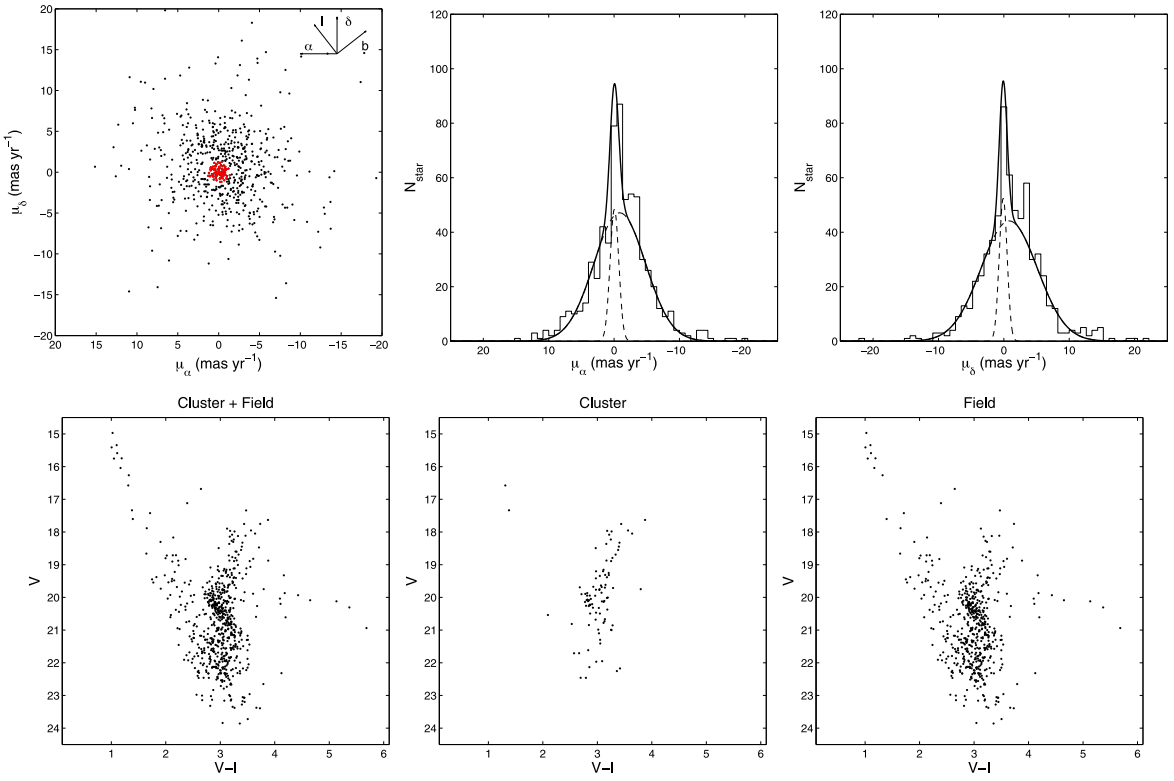

Figure 18. Proper motion and CMD decontamination of Terzan 2.

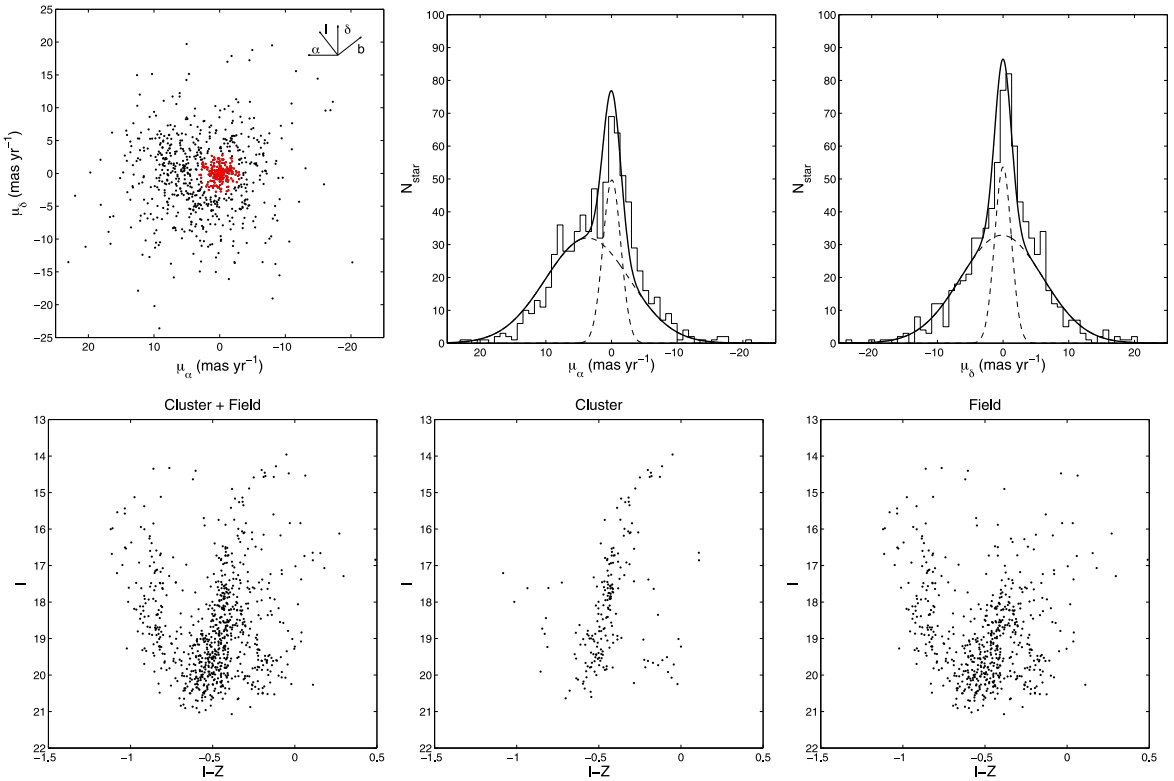

Figure 19. Proper motion and CMD decontamination of Terzan 4.

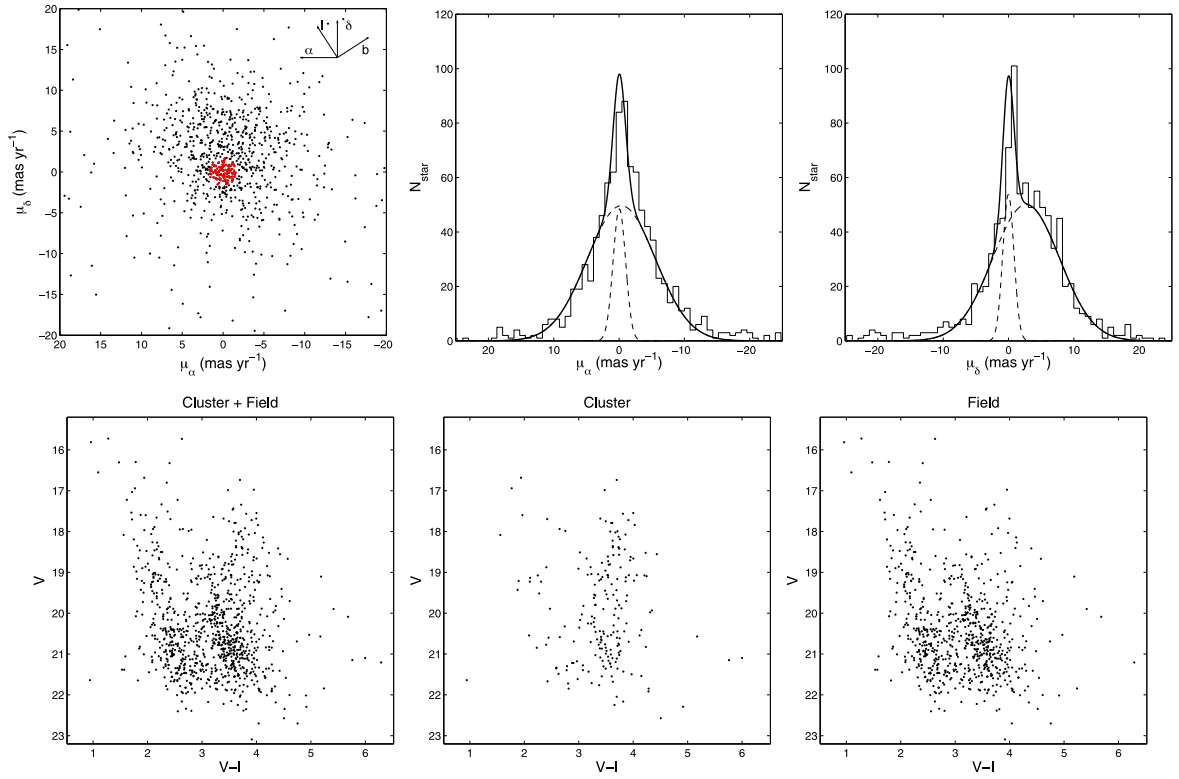

Figure 20. Proper motion and CMD decontamination of Terzan 9.

Terzan 9

Ortolani et al. (1999a) estimated a metallicity of [Fe/H] ~ -2.0, whereas Valenti et al. (2007) indicates [Fe/H] ~ -1.2. In the latter case, it could be added to the group of moderate metallicy and BHB clusters. Harris (1996, 2010 version) reports a radial velocity of 59 km s^{-1}. First and second epoch observations were obtained, respectively, with the DFOSC@Danish in 1998 July, and NTT+EFOSC2 in 2012 May. For this cluster, the time baseline is of 14 yr. It has a relatively high proper motion (Table 3, Fig. 20). Only a detailed orbital study can clarify if it is a halo or a bulge cluster.

NGC 6522

NGC 6522 is a moderately metal-poor GC projected on the Baade's Window. We derived the proper motion from two sets of observations: the first epoch images have been obtained with the Danish Telescope in 1992 June, and *HST*/WFPC2 in 1995 September, while the second epoch images come from NTT (2012 May). Both diagrams are well-cleaned, with *HST* first epoch including fainter stars. The dispersion of the proper motion plots is tighter for the Danish data, possibly due to the inclusion of fainter stars in the *HST* comparison. The abundance analysis and radial velocity of eight stars was presented in Barbuy et al. (2009, 2014). Its proper motion has been investigated also by Terndrup et al. (1998), who derived values with respect to a star at rest in the nuclear bulge equal to $(\mu_l, \mu_b) = (1.4 \pm 0.2, -6.2 \pm 0.2)$ mas yr^{-1}. The top six panels of Fig. 21 show the cluster proper motion obtained in this work. Our analysis produced the values $(\mu^*_\alpha,\ \mu_\delta) = (3.35 \pm 0.60,\ -1.19 \pm 0.34)$ mas yr^{-1}, corresponding to a proper motion in Galactic coordinates of $(\mu_l, \mu_b) = (0.4, -3.1)$ mas yr^{-1}. Our result is about a factor of 2 smaller than the one obtained by Terndrup et al. (1998). We also tried to derive its proper motion independently, by using archive *HST* images. The results are shown in the bottom six panels of Fig. 21. This new estimate of the proper motion of the cluster produced the value $(\mu_\alpha, \mu_\delta) = (3.6 \pm 0.6, -1.2 \pm 0.3)$ mas yr^{-1}, which is consistent with our previous analysis. Note that the calibration star from Terndrup et al. (1998) is outside our field. We finally also note that in Barbuy et al. (2014) a revised radial velocity of $v_r = -14.3 \pm 0.5$ km s^{-1} was obtained, which is basically compatible with the adopted value given in Table 3.

NGC 6558

NGC 6558 has a well-determined low proper motion, combined with a high radial velocity of -197.2 km s^{-1} (Barbuy et al. 2007). First and second epoch observations were obtained, respectively, at the NTT+EMMI in 1993 June, and NTT+EFOSC2 in 2012 May. The second epoch was obtained under exceptionally good seeing conditions. The present decontaminated CMD is very populous with well-defined sequences. The cleaning was effective in this case, superseding previous CMDs for this cluster, as shown in Fig. 22. Vásquez et al. (2013) found a value of the proper motion $(\mu_l \cos(b), \mu_b) = (0.30 \pm 0.14, -0.43 \pm 0.13)$ mas yr^{-1}. The present proper motion in Galactic coordinates is $(\mu_l \cos(b), \mu_b) = (0.37 \pm 0.43, 0.29 \pm 0.62)$ mas yr^{-1}. Considering the large errors relative to the small motion of the cluster, and that the telescopes and the techniques are different, the results are in a very good agreement. An orbit derivation is needed in order to establish its dynamics.

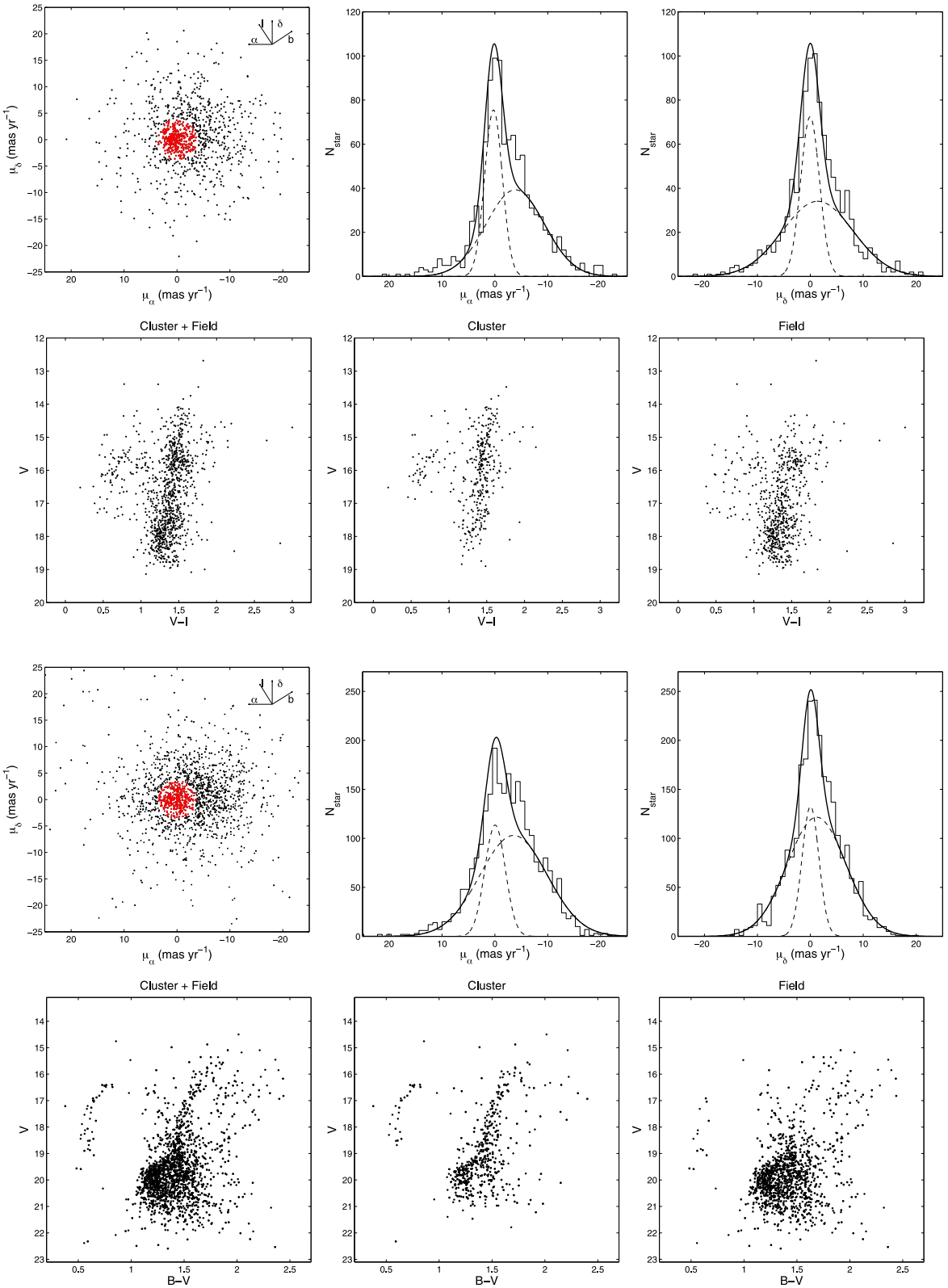

Figure 21. Proper motion and CMD decontamination of NGC 6522 from Danish Telescope – NTT and NTT – *HST* data.

NGC 6540

NGC 6540 has a detectable small proper motion, and the cleaning is effective, showing that we correctly identified the CMD features. A very low radial velocity of 17.2 km s^{-1} is given in Harris (1996, 2010 version). First and second epoch observations were obtained, respectively, with the direct CCD camera at the Danish telescope in 1990 June, and NTT+EFOSC2 in 2012 May. The observing

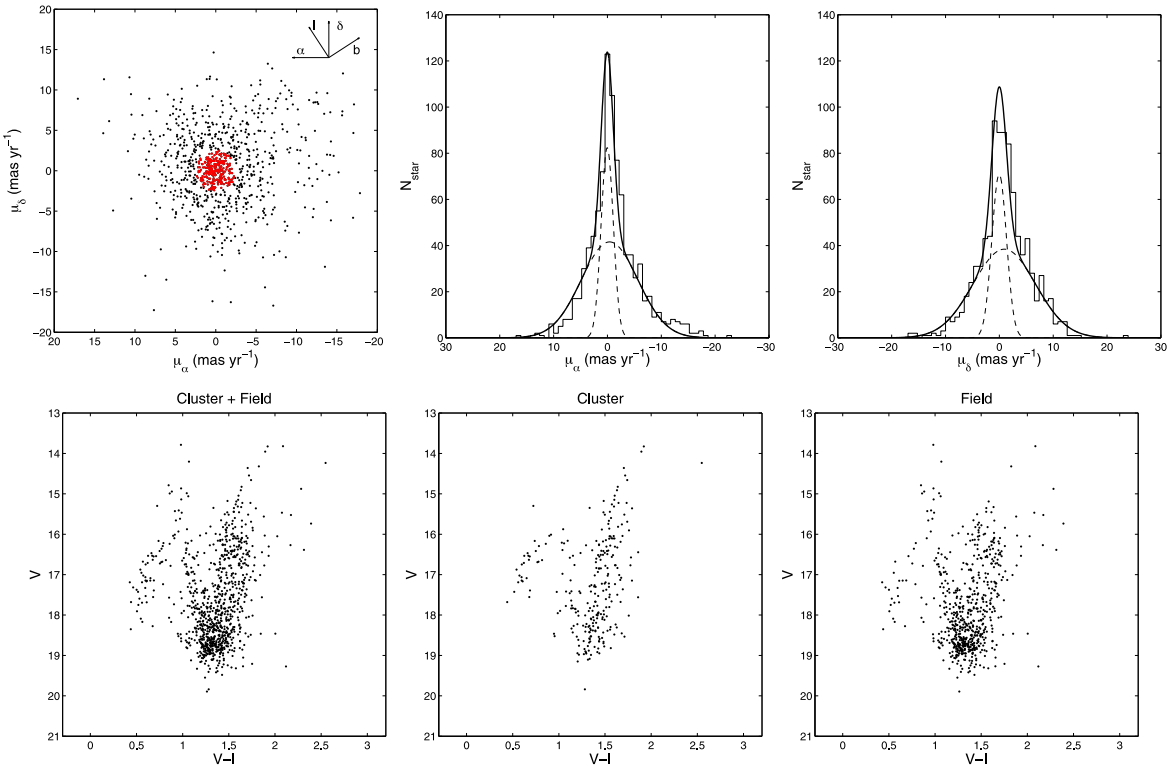

Figure 22. Proper motion and CMD decontamination of NGC 6558.

runs were the same as for Terzan 1. Given its low proper motion and radial velocity, the object could be near its apogalacticon. Bica et al. (1994) estimated a metallicity of [Fe/H] ~ -1.0. This could be another moderate metallicity cluster with a BHB. The proper-motion cleaning was not very effective, as shown by about the same number of BHB stars in the cluster and in the field, due to a very small difference between the main motion of the cluster and field stars. Nevertheless, the proper-motion dispersion of field stars is sizably larger than that of cluster members. We can clearly see that the CMD of proper-motion-selected stars (middle panel on the bottom of Fig. 23) is fairly free of field stars. Most of the field stars are indeed included in the bottom-right panel, where they should belong.

AL 3

First and second epoch observations were obtained respectively, with DFOSC@Danish telescope in 2000 March, and NTT+EFOSC2 in 2012 May. AL 3 shows a rather high right ascension proper motion as compared with the other central clusters, but it is comparable to that of the bulge edge cluster NGC 6652. The proper motion in declination on the other hand is clearly higher in NGC 6652 than in AL 3. A radial velocity measurement for AL 3 is needed for a kinematical diagnostic. As compared with Ortolani et al. (2006), a few stars in the RGB are missing in the present CMD, owing to saturation effects in the second epoch image. The proper-motion-cleaned CMD confirms that AL 3 is a BHB cluster, and the RGB indicates a moderate metallicity (Fig. 24).

ESO456−SC38

First and second epoch observations were obtained, respectively, with NTT+SUSI in 1994 May, and NTT+EFOSC2 in 2012 May. This cluster has a relevant proper motion. Despite this, the proper-motion cleaning did not produce a well-defined CMD, because of the loose structure of the cluster and a high differential reddening (Fig. 25). Preliminary radial velocity values of $\sim -160\,\mathrm{km\,s^{-1}}$ were obtained by S. Vásquez (in preparation).

Palomar 6

The proper motion of Palomar 6 was based on the longest time base of our sample, spanning 20 years. First and second epoch observations were obtained, respectively, with NTT+EMMI in 1993 June, and NTT+EFOSC2 in 2013 May. The second epoch was obtained with the highest available spatial resolution. It has a proper motion of around 3 mas year^{-1}. Harris (1996) reports a radial velocity of $190\,\mathrm{km\,s^{-1}}$, and Lee, Carney & Balachandran (2004) measured $180\,\mathrm{km\,s^{-1}}$. The cluster is very reddened with $E(B-V) = 1.33$, and its distance is compatible with a location near the Galactic centre. For this reason, high-velocity vectors are expected. The proper-motion cleaning was very effective (see lower panels in Fig. 26), disentangling the cluster from the bulge population. The proper-motion-cleaned CMD confirms that it is a 47 Tuc-like cluster, with a red HB (Lee et al. 2004).

NGC 6652

We added NGC 6652 to the sample for comparison purposes. This borderline bulge cluster is located at $l = 1\overset{\circ}{.}53$, $b = -11\overset{\circ}{.}38$. The edge of the bulge was defined to be at around 10° by Soto et al. (2014) and Rojas-Arriagada et al. (2014). Proper motions were derived from *HST* observations as reported by Sohn et al. (2014). We find that its kinematics is very different from the sample bulge clusters, because its orbit is much more extended in the halo, reaching apocentric distances up to 10 kpc from the Galactic centre.

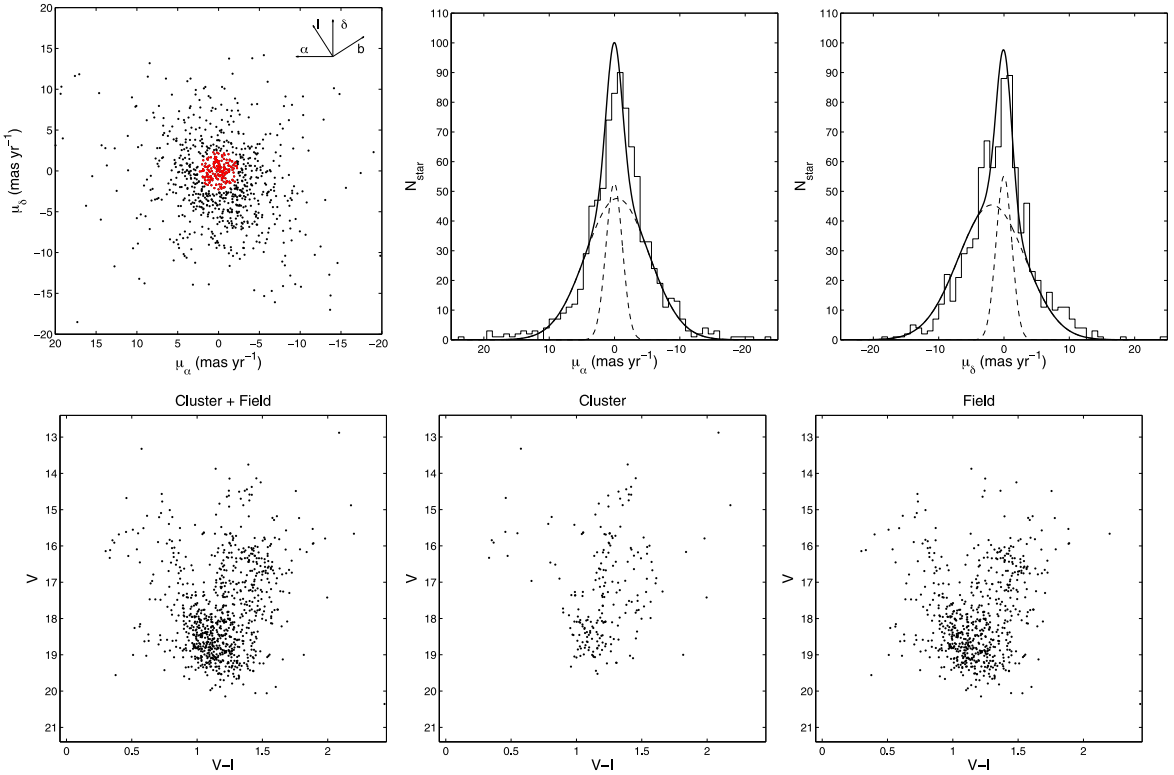

Figure 23. Proper motion and CMD decontamination of NGC 6540.

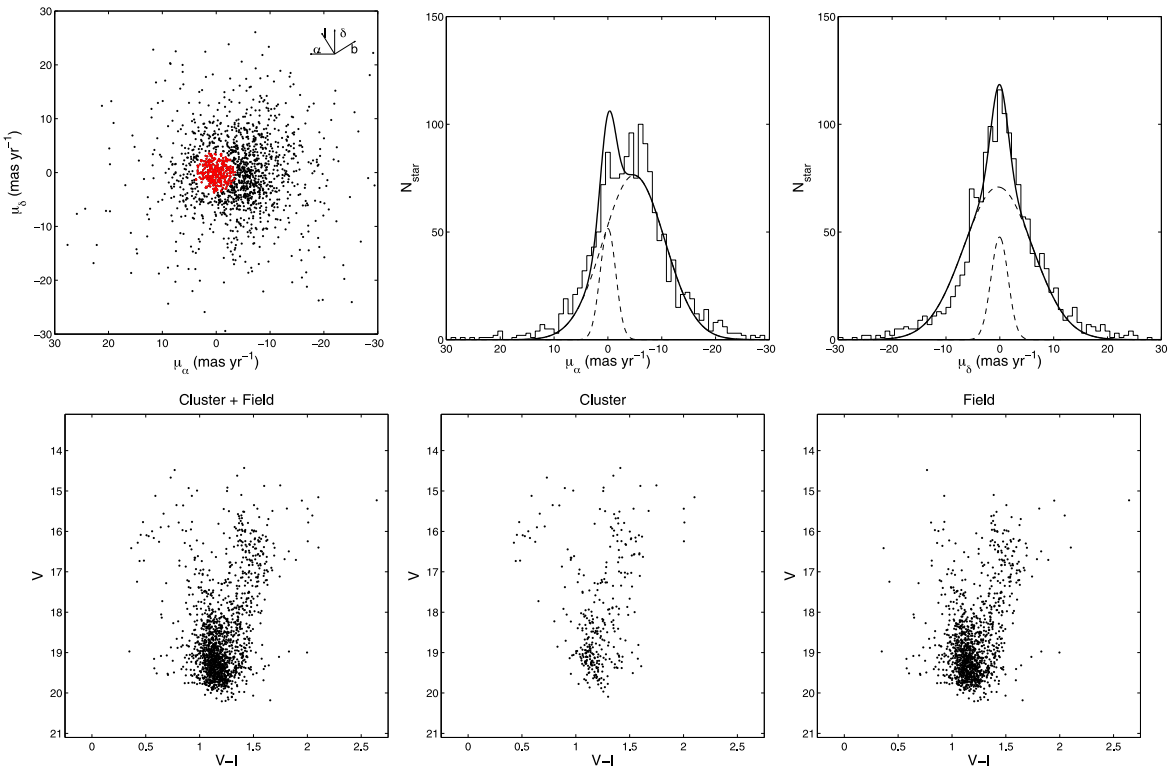

Figure 24. Proper motion and CMD decontamination of AL 3.

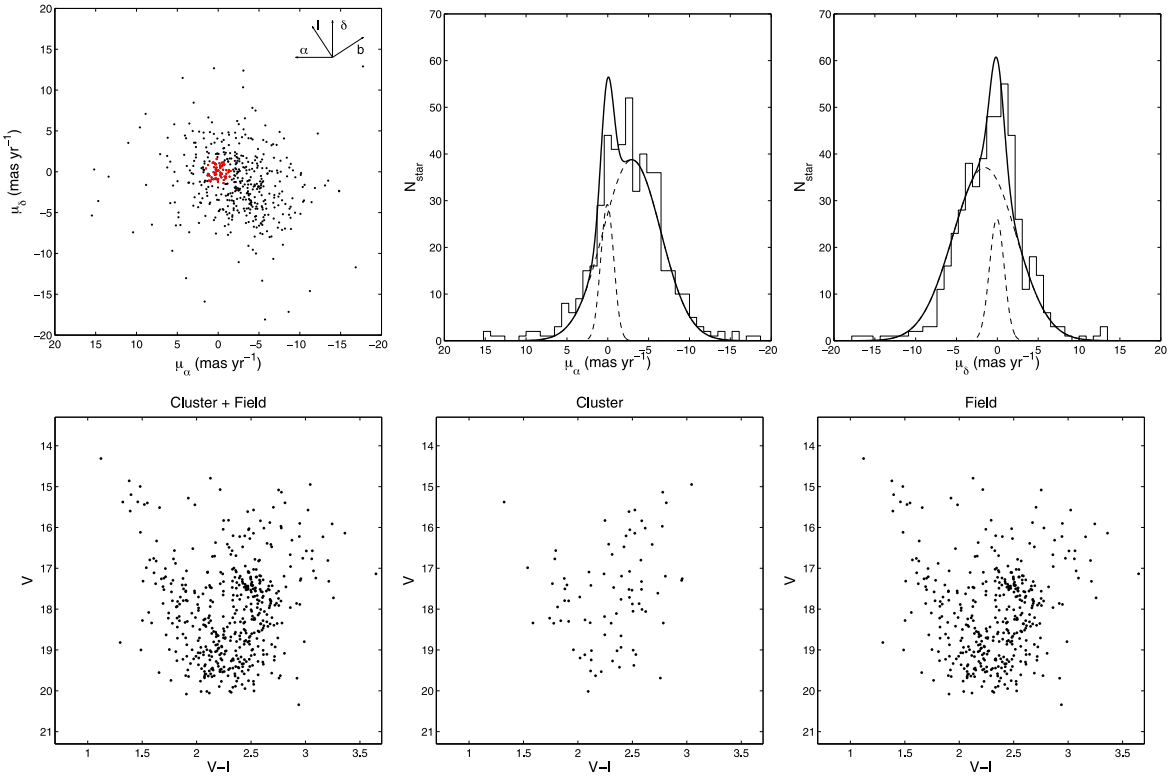

Figure 25. Proper motion and CMD decontamination of ESO456−SC38.

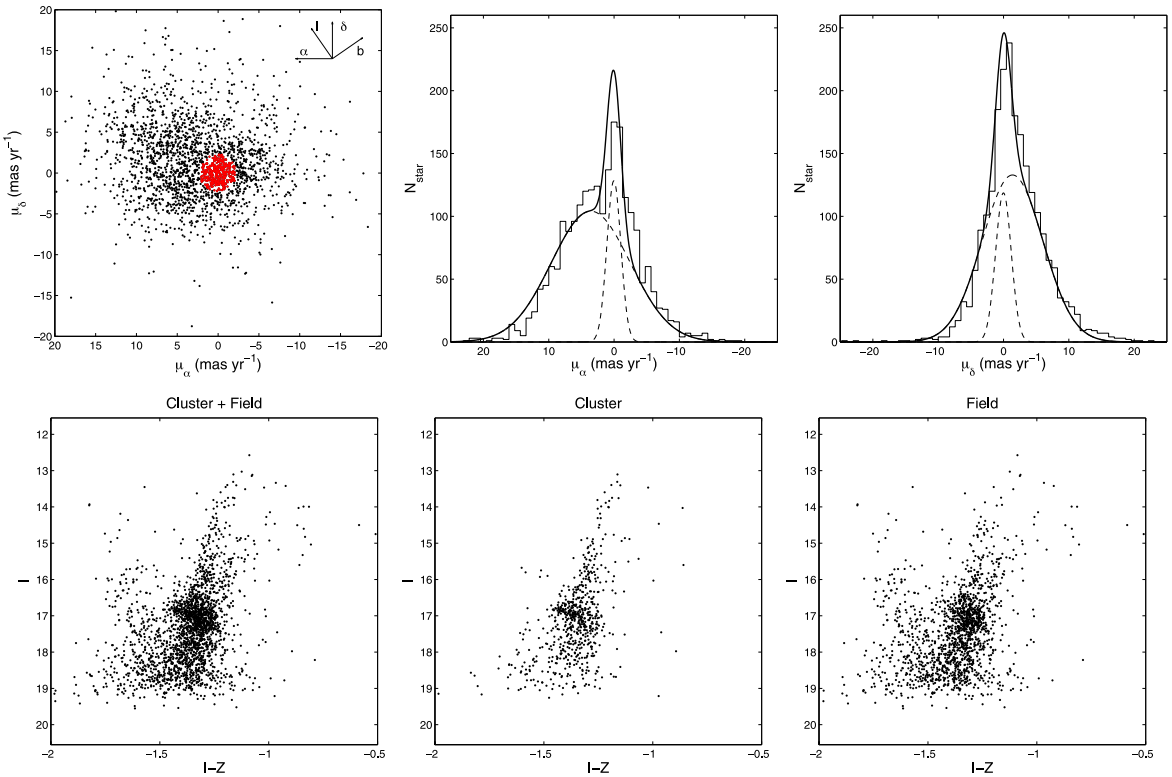

Figure 26. Proper motion and CMD decontamination of Palomar 6.

7 DISCUSSION AND CONCLUSIONS

We derived absolute proper motion values for 10 inner bulge GCs, thanks to first epoch images taken by our group in the 90 s, combined with recent dedicated observations at the ESO NTT telescope. The proper motions were computed from second epoch distortion-corrected positions using field stars as absolute reference frame.

The derived velocity components are as a rule very low suggesting that most of these clusters are trapped in the bulge and/or the bar. These clusters could have been formed earlier than the bar, and were later trapped inside it (Babusiaux et al. 2014). The low velocities are made evident, by a comparison with NGC 6652 (Sohn et al. 2014). This cluster is located near $b \sim 10^{\circ}$, a region considered by Soto et al. (2014) and Rojas-Arriagada et al. (2014) as the outer bulge. The bulge-halo transition is defined as the region where some bulge rotation is still detected for the field stars, but the ratio of metal-rich/metal-poor field stars components is inverted, with metal-poor stars (halo) prevailing outside this region. The comparison of the kinematics between our inner bulge sample clusters and NGC 6652 shows a clear difference in space velocities, indicating the central clusters to be a distinct population relative to the outer bulge/inner halo clusters. It would be important to acquire proper motions of other clusters in the external regions of the bulge.

Dinescu et al. (1999) found lower velocities for inner galaxy clusters as compared with outer halo ones. We found even lower velocities for inner bulge clusters.

In conclusion, the proper motion analysis of the present sample clusters indicates that the moderately metal-poor and metal-rich clusters appear to have preferentially low-velocity components. The halo contamination inside the bulge appears to be limited to very few objects, if any. The proper-motion-cleaned CMDs confirm a typical pattern for the Blue HB moderate metallicity clusters.

The orbits and their evolution will be presented in a forthcoming paper.

ACKNOWLEDGEMENTS

We are thankful to the referee for a careful reading and useful suggestions. We are grateful to S. Casotto for important clarifications on dynamical aspects. We are thankful to Y. Momany for helping with the observations. We thank V. Mezzalira for helpful technical support. LR acknowledges a CRS scholarship from Swinburne University of Technology. BB and EB acknowledge grants from the Brazilian agencies CNPq and Fapesp. SO acknowledges the Italian Ministero dell'Università e della Ricerca Scientifica e Tecnologica, and the financial support from the Università di Padova.

REFERENCES

Anderson J., King I. R., 2003, PASP, 115, 113
Babusiaux C. et al., 2010, A&A, 519, A77
Babusiaux C. et al., 2014, A&A, 563, A15
Barbuy B., Bica E., Ortolani S., 1998, A&A, 333, 117
Barbuy B., Ortolani S., Bica E., 1994, A&A, 285, 871
Barbuy B., Zoccali M., Ortolani S., Minniti D., Hill V., Renzini A., Bica E., Gómez A., 2007, AJ, 134, 1613
Barbuy B., Zoccali M., Ortolani S., Hill V., Minniti D., Bica E., Renzini A., Gómez A., 2009, A&A, 507, 405
Barbuy B. et al., 2014, A&A, 570, A76
Bellini A. et al., 2013, ApJ, 765, 32
Bica E., Ortolani S., Barbuy B., 1994, A&A, 283, 67
Bica E., Bonatto C., Barbuy B., Ortolani S., 2006, A&A, 450, 105
Bobylev V. V., Mosenkov A. V., Bajkova A. T., Gontcharov G. A., 2014, Astron. Lett., 40, 86
Brunthaler A. et al., 2011, Astron. Nachr., 332, 461
Cao L., Mao S., Nataf D., Rattenbury N. J., Gould A., 2013, MNRAS, 434, 595
Côté P., 1999, AJ, 118, 406
Dékány I., Minniti D., Catelan M., Zoccali M., Saito R. K., Hempel M., Gonzalez O. A., 2013, ApJ, 776, L19
Di Matteo P. et al., 2014, A&A, 567, A122
Dinescu D. I., Girard T. M., van Altena W. F., 1999, AJ, 117, 1792
Dinescu D. I., Girard T. M., van Altena W. F., López C. E., 2003, AJ, 125, 1373
Do T. et al., 2013, ApJ, 779, L6
Feltzing S., Johnson R. A., 2002, A&A, 385, 67
Ferraro F. R. et al., 2009, Nature, 462, 483
Gillessen S., Eisenhauer F., Trippe S., Alexander T., Genzel R., Martins F., Ott T., 2009, ApJ, 692, 1075
Harris W. E., 1996, AJ, 112, 1487
Hou L. G., Han J. L., 2014, A&A, 569, A125
Idiart T. P., Barbuy B., Perrin M.-N., Ortolani S., Bica E., Renzini A., 2002, A&A, 381, 472
Irrgang A., Wilcox B., Tucker E., Schiefelbein L., 2013, A&A, 549, A137
Johnson D. R. H., Soderblom D. R., 1987, AJ, 93, 864
Kinman T. D., 1959, MNRAS, 119, 538
Kuijken K., Rich R. M., 2002, AJ, 124, 2054
Lee J.-W., Carney B. W., Balachandran S. C., 2004, AJ, 128, 2388
Malkin Z. M., 2013, Astron. Rep., 57, 128
Morgan W. W., 1959, AJ, 64, 432
Nishiyama S. et al., 2006, ApJ, 647, 1093
Origlia L., Rich R. M., 2004, AJ, 127, 3422
Ortolani S., Bica E., Barbuy B., 1994, A&A, 286, 444
Ortolani S., Bica E., Barbuy B., 1995, A&A, 296, 680
Ortolani S., Bica E., Barbuy B., 1997a, A&AS, 126, 319
Ortolani S., Barbuy B., Bica E., 1997b, A&A, 319, 850
Ortolani S., Bica E., Barbuy B., 1997c, A&A, 326, 614
Ortolani S., Bica E., Barbuy B., 1999a, A&AS, 138, 267
Ortolani S., Bica E., Barbuy B., 2006, ApJ, 646, L115
Ortolani S., Barbuy B., Bica E., Renzini A., Marconi G., Gilmozzi R., 1999b, A&A, 350, 840
Ortolani S., Barbuy B., Bica E., Zoccali M., Renzini A., 2007, A&A, 470, 1043
Ortolani S., Barbuy B., Momany Y., Saviane I., Bica E., Jilkova L., Salerno G. M., Jungwiert B., 2011, ApJ, 737, 31
Pichardo B., Martos M., Moreno E., 2004, ApJ, 609, 144
Pichardo B., Martos M., Moreno E., Espresate J., 2003, ApJ, 582, 230
Piotto G. et al., 2002, A&A, 391, 945
Reid M. J. et al., 2014, ApJ, 783, 130
Rich R. M., Ortolani S., Bica E., Barbuy B., 1998, AJ, 116, 1295
Rojas-Arriagada A. et al., 2014, A&A, 569, A103
Schönrich R., 2012, MNRAS, 427, 274
Schönrich R., Binney J., Dehnen W., 2010, MNRAS, 403, 1829
Sohn S. T., van der Marel R. P., Carlin J. L., Majewski S. R., Kallivayalil N., Law D. R., Anderson J., Siegel M. H., 2014, preprint (arXiv: 1408.3408)
Soto M., Zeballos H., Kuijken K., Rich R. M., Kunder A., Astraatmadja T., 2014, A&A, 562, A41
Stetson P. B., 1987, PASP, 99, 191
Terndrup D. M., Popowski P., Gould A., Rich R. M., Sadler E. M., 1998, AJ, 115, 1476
Valenti E., Ferraro F. R., Origlia L., 2007, AJ, 133, 1287
Vásquez S. et al., 2013, A&A, 555, A91
Zinn R., 1985, ApJ, 293, 424
Zoccali M., Renzini A., Ortolani S., Bica E., Barbuy B., 2001, AJ, 121, 2638
Zoccali M. et al., 2014, A&A, 562, A66

This paper has been typeset from a TEX/LATEX file prepared by the author.